Title

Quantum Monte Carlo Calculations of Scattering

Author

Flores, Abraham R.

Publication Date

2023

UNIVERSITY OF CALIFORNIA,
IRVINE

Quantum Monte Carlo Calculations of Scattering

DISSERTATION

submitted in partial satisfaction of the requirements
for the degree of

DOCTOR OF PHILOSOPHY

in Computational Science

by

Abraham R. Flores

Dissertation Committee:
Professor Kenneth M. Nollett, Chair
Professor Filipp Furche (UCI)
Professor Calvin Johnson (SDSU)
Professor Manoj Kaplinghat (UCI)
Professor Shaul Mukamel (UCI)

2023

DEDICATION

To Liz

TABLE OF CONTENTS

LIST OF FIGURES

Page

LIST OF TABLES

ACKNOWLEDGMENTS

For those of you reading this, thank you. As I sit here today, I can only think of the tremendous support I have received. To my brothers, Noah, Zach, Eli, and Logan, thank you for always having my back. To my parents, Mary and Josè, to their parents, thank you for all the love and devotion. To my family, related or not, you have made my dreams possible; thank you. For my mentors, teachers, professors, and coaches, thank you for pushing me to become a better person and scientist. To Ken, whose brilliance I have seldom seen matched, thank you for all your time and energy. To Bob, thank you for your immense contribution to quantum Monte Carlo methods and for being an excellent mentor. To Maria, thank you for being an inspiring role model and exemplary teacher. To Mark, thank you for bringing me into the field of computational nuclear physics; you were one of the first people in my life to allow me to shine. To my friends, who kept me a sane exile over the years, thank you for all the memes and terrible DPS. To my Michigan State physics nerds, Dustin and Colin, thank you for being a friend when I had so few. To my CSRC classmates, thank you for making it a delight to come to campus. To my Phoenix family, thank you for always being ready to have a good time. Lastly, to Liz, my partner, my world, thank you for everything you have given us. Thank you for making my life an absolute joy and constantly pushing me to be the best version of myself.

* I would like to thank A. Kievsky for assistance in understanding scattering-matrix conventions, M. Paris and G. Hale for explanations of the R-matrix phase shifts, and R. Lazauskas for quickly providing published Faddeev-Yakubovsky results.

* I acknowledge and have obtained permission from Kenneth M. Nollett to use the work of our Phys. Rev. C journal submission (ArXiv:2209.00093) in this dissertation.

* This work was supported by the US Department of Energy, Office of Nuclear Physics, Award DE-SC0019257. The many-body calculations were performed on the parallel computers of the Laboratory Computing Resource Center, Argonne National Laboratory, and the computers of the Argonne Leadership Computing Facility via the INCITE grant "Ab-initio nuclear structure and nuclear reactions."

VITA

Abraham R. Flores

EDUCATION

Doctor of Philosophy in Computational Science	**2023**
University of California, Irvine	*Irvine, California*
Bachelor of Science in Physics	**2017**
Michigan State University	*East Lansing, Michigan*

RESEARCH EXPERIENCE

Graduate Research Assistant	**2017–2023**
San Diego State University	*San Diego, California*
Student Intern	**2021–2021**
NASA Langley	*Hampton, Virginia*
Undergraduate Research Assistant	**2016–2017**
NSCL/FRIB	*East Lansing, Michigan*
Undergraduate Research Assistant	**2016–2016**
Notre Dame University	*South Bend, Indiana*

JOURNAL SUBMISSIONS

Variational Monte Carlo Calculations of $n + {}^3$H Scattering **2023**

ArXiv:2209.00093 [nucl-th] (2023), Submitted to Phys. Rev. C

TALKS

Variational Monte Carlo Calculations of $n + {}^3$H Scattering **Oct 2022**

APS Division of Nuclear Physics Fall Meeting, New Orleans, LA

Variational Monte Carlo Calculations of $n + {}^3$H Scattering **Sept 2022**

Nuclear Physics Seminar at Washington University in St. Louis

ABSTRACT OF THE DISSERTATION

Quantum Monte Carlo Calculations of Scattering

By

Abraham R. Flores

Doctor of Philosophy in Computational Science

University of California, Irvine, 2023

Professor Kenneth M. Nollett, Chair

A paramount goal in nuclear physics is to unify *ab-initio* treatments of bound and unbound states. The position-space quantum Monte Carlo (QMC) methods have a long history of successful bound-state calculations in light systems but have seen minimal implementation in unbound systems. Here I introduce a numerical method to improve the efficiency and accuracy of unbound-state calculations in QMC, implement it numerically in the definitive computer codes for these methods, and test it out in nuclear systems small enough for quick turnaround but large enough to have interesting dynamics. The method involves inferring long-range amplitudes in the wave function from integrals over the small region where all the particles interact. This approach using integral relations is well established in the literature; here, I develop it for the QMC framework in both variational Monte Carlo (VMC) and Green's function Monte Carlo (GFMC) calculations. The integral method produces more accurate scattering observables in neutron-^{3}H scattering for VMC wave functions than direct evaluation from the same variational wave function. Applying the integral method in Green's function Monte Carlo reproduces existing results in neutron-alpha scattering, clearing the way for its use in coupled-channels problems. Establishing these methods reduces the amount of human effort needed for a specified level of precision. It clears the way for GFMC-accurate calculations of coupled-channels scattering, including reactions, in nuclear mass ranges that may be permanently beyond the range of the other few-body methods.

Chapter 1

Introduction

In recent years there has been a growing call for *ab-initio* calculations of unbound nuclear systems; such calculations constitute half of the acknowledged goal of unifying the treatment of bound and unbound systems in nuclei [1, 2]. The work for bound systems is far ahead of that for unbound systems, because unbound systems are significantly harder to treat. For example, the observables one computes in unbound systems do not trivially reduce to eigenvalue or Rayleigh-Ritz problems. Additionally, the solution of unbound systems by basis-function expansion is much more expensive than comparable bound systems. Beyond mass-4 systems, these hurdles are rarely overcome due to the required basis drastically growing with the number of particles. This has resulted in the development of *ab-initio* methods, mainly in the context of bound states.

Developing methods for computing nuclear systems goes hand in hand with developing nuclear representations of the nucleon-nucleon interaction. Mass-4 and -5 systems are computationally efficient testing grounds for methods to compute unbound systems. Regarding physical interest, the $A = 4$ and $A = 5$ are some of the smallest systems available to probe three-body forces. Additionally, both systems are well-benchmarked by existing computational methods in calculations that use some of the same nuclear potentials available to Quantum Monte Carlo (QMC) methods. Comparison against the benchmarks generates instant numerical and systematic feedback at a near-zero computational cost.

Benchmarks for the $A = 4$ systems have been published [3, 4], using the Faddeev-Yakubovsky equations (FY) [5–10], the Alt-Grassberger-Sandhas equations (AGS) [11–19], and the Hyperspherical Harmonic (HH) method [20–24]. As for $A = 5$, to my knowledge, the only neutron-alpha phase shifts that have been computed with the Argonne v_{18} (AV18) potential are the GFMC results from Ref. [25] and the calculations using the FY equations in Ref. [9]. Those computations are a reliable benchmark for applying new methods to n-alpha.

QMC methods have succeeded in computing bound states for systems up to carbon-12 to within 1-2% of experimental results [26] and accurately computed infinite matter [27, 28]. Recently, there has been a renewed push to go to larger nuclei ($A > 12$). This work greatly benefits from that push from code speed-up, which enables more calculations with QMC methods in unbound systems, as they are significantly more expensive to map the entire energy dependence of observables for the system. This work aims to enable QMC methods to compute unbound systems for systems beyond mass-4. However, the mass-4 and -5 systems now serve as an efficient testing environment for method development.

The few studies of nuclear scattering with QMC published so far are all based on representing continuum states as particle-in-a-box states and have not included coupled-channels cases. The first iterations of this technique in Refs. [29, 30] used the variational Monte Carlo (VMC) method to compute proton + ^{3}H and neutron + ^{4}He, respectively. In Ref. [25], the Green's function Monte Carlo (GFMC) method was used to compute energies and phase shifts of particle-in-a-box wave functions in n+^{4}He, scattering. The same system and method were revisited in [31] to analyze new nuclear potentials. In this thesis, I seek to reduce the difficulty of QMC scattering calculations by implementing well-established relations between the short-range wave function and scattering properties. I refer to the resulting method as the “integral method,” closely related to the Lippmann-Schwinger equation. This method is similar to the source term calculations of [32, 33], the aysmptotic normalization coefficent (ANC) calculations of [34–38], and the scattering calculations of [22–24, 39, 40].

The integral methods are techniques for obtaining accurate information from wave functions that have already been computed. Accordingly, my work to develop them begins with the computation of n-triton and n-alpha scattering states as particle-in-a-box problems. Specifying the logarithmic derivative of the wave function at the surface of a spherical box makes the kinetic energy operator Hermitian so that the ground state of the box can be found by an energy minimization procedure. For single-channel scattering, the S-matrix can be directly computed from the energy and the boundary condition in what I call the direct procedure. This procedure requires that the outer parts of the wave function are accurate, so that the relationship between the measurable region and interaction region is correct. In VMC, it is challenging to construct a variational ansatz that works well in the outer parts of the box. Although GFMC is more accurate than VMC, it has difficulties in the outer parts of wave functions [25]. Once the wave function exists, the integral method fully utilizes the well-computed short-range wave function to compute surface amplitudes similar to ANCs from integrals throughout the box. These amplitudes explicitly determine the S-matrix.

I demonstrate the implementation of the integral methods in VMC by computing neutron-triton scattering. The first step in this procedure is an internal verification of the integral relations by comparing spectroscopic overlaps computed by direct sampling and by the integral relations. Additionally, I use these overlaps to choose a regularization parameter unambiguously, which cannot be chosen by energy minimization. Lastly, I introduce the fixed interior wave (FIW) approximation, a procedure for computing the full low-energy ($E_{\text{lab}} \leqslant 10$ MeV) dependence of the S-matrix using only a single VMC wave function. Using the integral method in VMC with the FIW approximation, I compute the first few relevant channels in ${}^3\text{H}(n,n)^3\text{H}$ for both traditional r-space potentials and more modern chiral potentials and compare against available benchmarks. The scattering cases include single- and coupled-channel problems; for QMC, I present the first coupled-channel scattering results. I also compute near-threshold n-trition scattering observables and discuss the observed relationship to the triton binding energy.

The next step in developing the QMC integral methods is implementing the integral relations in GFMC. Because adding the correct spin dependence for the neutron-triton system in GFMC would have taken away from limited development time, I decided to test, apply and benchmark the GFMC integral method to $^4\text{He}(n,n)^4\text{He}$. In developing the integral relations for GFMC, I started from existing GFMC spectroscopic overlap routines [41]. The critical task is to develop routines that compute the nuclear potential acting on the $n+{}^4\text{He}$ clusterized wave function. After this implementation, I present and benchmark the GFMC integral method to the previous GFMC calculations of Ref. [25] and the FY calculations of Ref. [9].

In the $n+{}^4\text{He}$ calculations, I propose adjusting the fixed interior wave approximation (FIW) by computing actual wave functions on a sparse grid in energy. Then I interpolate the results over a dense grid between those wave functions through the FIW approximation. Although I do not prove this interpolation scheme is explicitly correct, I demonstrate that the fixed interior wave interpolation (FIWI) maintains the trend established in integral method calculations.

The remainder of this dissertation is organized as follows. In Chapter 2, I describe my notation and connect it to the formalisms used in the literature. In Chapter 3, I describe the QMC wave functions and their adaptation to scattering states. In Chapter 4, I describe how to extract scattering amplitudes and spectroscopic overlaps from the wave function using both the "direct" and "integral" procedures in single- and coupled-channel cases. In Chapter 5, I compare the overlap functions computed by the two procedures, interpret the output of the integral method, and use the results to select the regularization parameter needed in the integral calculations. I also introduce the fixed interior wave approximation. In Chapter 6, I demonstrate the successful use of the integral method with VMC wave functions by computing overlaps and scattering observables of the neutron-triton system. I then present $n + {}^4$He GFMC single channel phase shifts and compare them with available benchmarks. In Chapter 7, I summarize my findings and discuss their implications for the future.

Chapter 2

Introduction to Scattering

This section outlines the necessary mathematical framework to describe single-nucleon scattering. Specifically, I describe how one relates theoretical descriptions of scattering theory to experimental results. I also describe my two-body scattering notation and how to extrapolate low-energy experiments to threshold to determine scattering lengths. In this chapter I draw extensively from the introductory information in Ref. [42].

2.1 Theory and Experiment

Scattering experiments deal with particles that come from infinity and escape to infinity. It is usually convenient to define the energy of a system so that it is zero when the kinetic energy is zero and the projectile is infinitely far from the target; then, scattering always involves positive energy states. Since the particles can escape to infinity, a fixed energy wave function fills all of space and constitutes an open quantum system. The experimental results depend on the amplitudes of the wave function at infinity.

The prototypical setup for scattering experiments starts with a collimated beam of projectiles that all have the same energy and directs them onto a target containing many nuclei. When it reaches the target, the projectile can collide with a target nucleus through the nuclear and Coulomb interactions and scatter in some other direction of travel. When a detector is placed near the target at some angle away from the initial beam, the number of projectiles deflected in that direction can be measured. The number of particles detected will depend on both the scattering angle and the solid angle subtended by the detector as seen from the target, $\Delta\Omega$ (assumed to be small). The detection rate per target nucleus dN/dt is then related to the incoming flux of projectiles j_{inc} by

$$\frac{dN}{dt} = j_{\text{inc}} \frac{d\sigma}{d\Omega}(\theta, \phi)\Delta\Omega. \tag{2.1}$$

A counting experiment then allows the experimenter to map out the differential cross section ($d\sigma/d\Omega$) as a function of projectile energy. The differential cross section relates the incoming flux of projectiles to the scattered flux of particles in a given angular direction. The total cross section σ_T specifies the total fraction of projectiles that are deflected per target nucleus and is found by integrating the differential cross section over all angles.

In terms of wave functions, there is an initial incoming wave function $\psi(\mathbf{r})$ that depends on the vector separation $\mathbf{r}$ of the projectile from the target. Incoming projectiles in a beam of given energy constitute a plane wave along the polar axis, $\psi(\mathbf{r}) = e^{ikz}$, where the wave number $k^2 = 2m/\hbar^2 E_{\text{cm}}$, and E_{cm} is the energy of the system in the center-of-mass frame. The unscattered particles remain part of the plane wave. However, scattered particles form a spherical wave propagating outward from the target, like waves moving out of a disturbance in a pond surface, precisely analogous to Huyghens' principle. The asymptotic wave function is then a superposition of the original plane wave with an outgoing spherical scattered wave,

$$\lim_{r\to\infty} \psi(\mathbf{r}) = e^{ikz} + \frac{e^{ik\mathbf{r}}}{|\mathbf{r}|} f(\theta, \phi), \tag{2.2}$$

where I have introduced the angular function $f(\theta, \phi)$ referred to as the scattering amplitude. It describes the magnitude and phase of the current in the scattered beam. The scattering amplitude is the fundamental bridge between theory and experiment. We can see this through the conservation of probability current, which gives the following relation for the scattered flux,

$$j_{\text{scat}}(r) = j_{\text{inc}} \frac{|f(\theta, \phi)|^2}{r^2} + \mathcal{O}(r^{-3}). \tag{2.3}$$

By using this relation in Eq. 2.1 and ignoring the additional terms because the detector is effectively at infinity, we are able to relate the differential cross section to the scattering amplitude,

$$\frac{d\sigma}{d\Omega} = |f(\theta, \phi)|^2. \tag{2.4}$$

Once the scattering amplitude is computed, the cross section follows. The main goal in theoretical calculations is to establish the relationship between different parts of the wave function embodied in $f(\theta, \phi)$. From there, outcomes of all scattering experiments can be predicted, including their dependence on projectile energy.

It is useful to expand the entire wave function into a sum over partial waves that each have definite values of all angular momentum quantum numbers. For a partial wave of given orbital angular momentum L, the radial dependence at large r can be written in terms of a pair of known linearly independent functions instead of the pair in Eq. 2.2. Partial waves are more conveniently calculated than the whole wave function, and their individual contributions to the scattering amplitude can be read out of their large r regions.

For low-energy scattering, only the partial waves with the smallest values of angular momentum contribute to the scattered wave. Each partial wave constitutes a “channel” through which probability can “flow,” and I label them in two ways. The first way is by the total angular momentum and parity (J^π), which are both conserved by the nuclear Hamiltonian. In addition to J^π, I label channels by orbital angular momentum L and spin angular momentum S (which can be changed by our interaction), using Russell-Saunders notation ${}^{2S+1}L_J$. For some J^π, there is only one channel, but for others (e.g., ${}^3S_1$ and ${}^3D_1$), there are two. In the multiple-channel case, the incoming and outgoing channels can differ, and we have a coupled-channel problem. This can result from the tensor term of the strong force, which mixes channels of the same parity but with $L = J \pm 1$. In the systems examined below, I also have a case of significant mixing between channels of the same L and J but different S due to spin-flip operators in the potential.

2.2 Two-Body Scattering

In two-cluster scattering there are three common representations of the asymptotic wave function. In these, wave function amplitudes at infinity are related to each other by the T-, S-, or K-matrix, depending on whether the incoming wave function is represented by plane, spherical, and/or standing waves.

In all of these, projecting the wave function into a specific channel at large radius gives a result that can be written in terms of solutions to the Coulomb wave equation. This is a radial Schrödinger equation with a Coulomb potential and positive energy, and in dimensionless form it is

$$-\frac{d^2u_l}{d\rho^2} + \left(\frac{l(l+1)}{\rho^2} + \frac{2\eta}{\rho}\right) u_l = u_l. \tag{2.5}$$

Here $\rho = k_c r_c$, while the Sommerfeld parameter is given in terms of charges Z_1e and Z_2e and the reduced mass μ by $\eta = Z_1Z_2e^2\mu/(\hbar^2 k_c)$. The channel wave number is given in terms of the channel energy E_c by $k_c^2 = 2\mu E_c/\hbar^2$. Real-valued independent solutions of Eq. (2.5) are the usual regular $F_l(\eta,\rho)$ and irregular $G_l(\eta,\rho)$ Coulomb functions [43]. (For neutron scattering $\eta = 0$, and these reduce to spherical Bessel functions; I will retain the more general notation of the Coulomb functions.) Outside the interaction region, the wave function may be written in terms of products of these functions with wave functions for the individual colliding nuclei, coupled to specified angular-momentum quantum numbers. These products form the regular and irregular channel-cluster functions

$$\mathcal{F}_c = \Psi^c_{1\otimes 2} \frac{F_{l_c}(\eta_c, k_c r_c)}{k_c r_c} \tag{2.6}$$

and

$$\mathcal{G}_c = \Psi^c_{1\otimes 2} \frac{G_{l_c}(\eta_c, k_c r_c)}{k_c r_c}. \tag{2.7}$$

I define the channel product function of cluster wave functions ψ_{1c} and ψ_{2c} with specified angular momentum in channel c as

$$\Psi^c_{1\otimes 2} = \mathcal{A}_c \left[\psi^{J_{1c}}_{1c} \otimes \left[\psi^{J_{2c}}_{2c} \otimes Y_{l_c}(\hat{r}_c) \right]_{j_c} \right]_J . \tag{2.8}$$

The operator $\mathcal{A}_c$ antisymmetrizes the function with respect to the partitions of the nucleons into the two clusters of channel c, which have wave functions $\psi^{J_{1c}}_{1c}$ and $\psi^{J_{2c}}_{2c}$. The angular momentum coupling in Eq. (2.8) organizes the spin and orbital angular momenta (J_{2c} and l_c) of cluster 2 to total j_c (corresponding to "jj coupling" when cluster 2 is a single nucleon as in my case.) This is then coupled to the angular momentum J_{1c} of cluster 1, which in my case is either a triton with $J = 1/2$ or an alpha particle with $J = 0$.

Of the standard scattering-matrix formulations, the one written entirely in terms of standing waves is the K-matrix, where the long-range part of the wave function is written as

$$\Psi(\text{all } r_c \to \infty) = \sum_c \left(A_c \mathcal{F}_c + B_c \mathcal{G}_c \right). \tag{2.9}$$

The amplitudes A_c and B_c determine all scattering observables, so the task of theoretical calculations is to find relations among them across all channels. Alternatively, the same function can be written in terms of incoming plane-wave components and outgoing spherical waves $\mathcal{H}_c^+ = \mathcal{G}_c + i\mathcal{F}_c$ to obtain the T-matrix formalism, where schematically

$$\Psi(\text{all } r_c \to \infty) = \sum_c \left(\mathscr{A}_c \mathcal{F}_c + \mathscr{B}_c \mathcal{H}_c^+\right) \tag{2.10}$$

and the surface amplitudes are $\mathscr{A}_c$, $\mathscr{B}_c$. Finally, the S-matrix formalism is written in terms of incoming and outgoing spherical waves $\mathcal{H}_c^\pm$ (with $\mathcal{H}_c^\pm = \mathcal{G}_c \pm i\mathcal{F}_c$) so that

$$\Psi(\text{all } r_c \to \infty) = \sum_c \left(\alpha_c \mathcal{H}_c^- + \beta_c \mathcal{H}_c^+\right); \tag{2.11}$$

in this case the amplitudes are α_c and β_c.

All of these formulations are equivalent and can be interconverted. When each set of amplitudes is written as a column vector, the relation between them is a matrix that predicts scattering outcomes by relating incoming to outgoing amplitudes:

$$\mathbf{B} = \hat{K}\mathbf{A} \tag{2.12}$$

$$\mathscr{B} = \hat{T}\mathscr{A} \tag{2.13}$$

$$\beta = \hat{S}\alpha. \tag{2.14}$$

Regardless of the form chosen, the amplitude vectors in Eqs. (2.12)-(2.14) can in principle be read out of any wave function solution and the scattering matrices found by inverting these equations, a process that requires N_c linearly independent wave functions if there are N_c coupled channels. Each formalism provides a natural way to view some calculations.

Because the particle number is conserved, single-channel scattering satisfies the constraint $|\alpha| = |\beta|$ and allows scattering matrices (actually scalars in this case) to be written in terms of a phase shift δ. Then $K = \tan\delta$, $T = e^{i\delta}\sin\delta$, and $S = e^{2i\delta}$. In multichannel scattering, each matrix has dimension $N_c \times N_c$, where N_c is the number of open channels. For $n +$ ^{3}H scattering each matrix is block-diagonal and splits into 1×1 and 2×2 blocks with definite parity π and total angular momentum J. For n-alpha, channel spin is 1/2 and there is no possibility of coupled channels if parity is conserved. For comparability with the literature, I report results in terms of channels defined by orbital quantum number L and by coupling neutron and triton spins to total spin quantum number S (instead of the l_c and j_c of Eq. 2.8). In this basis, the 2×2 coupled pairs of channels either have $L = J \pm 1$ or else have $S = 0, 1$ together with $L = J$. For these cases, I write the 2×2 S-matrix block in the Blatt-Biedenharn or eigenphase representation [44] as

$$\hat{S} = \hat{O}^T \begin{pmatrix} e^{2i\delta_-} & 0 \\ 0 & e^{2i\delta_+} \end{pmatrix} \hat{O}, \tag{2.15}$$

where

$$\hat{O} = \begin{pmatrix} \cos \epsilon^{J\pi} & \sin \epsilon^{J\pi} \\ -\sin \epsilon^{J\pi} & \cos \epsilon^{J\pi} \end{pmatrix}. \tag{2.16}$$

In the absence of channel mixing, $\hat{O}$ is the identity matrix and the $\delta_\pm$ are the phase shifts associated with the L channels $L = J \pm 1$ (when $L \neq J$) or with the spin channels $S = 0, 1$ (when $L = J > 0$). Each 2×2 block has a mixing parameter $\epsilon^{J\pi}$ that specifies the degree of channel mixing. Since $\delta_\pm$ are defined by eigenvalues of $\hat{S}$, they are independent of the angular momentum coupling scheme; $\epsilon^{J\pi}$ is not. Converting the amplitudes of Eqs. (2.9)-(2.11) from the jj coupling of Eq. (2.8) to the customary LSJ scheme for scattering is a straightforward exercise in Racah coefficients.

Because any pair of linearly independent solutions to Eq. (2.5) can be used to describe the asymptotic region in a given channel, it is straightforward to write the various scattering matrices in terms of each other [45] as follows:

$$\hat{T} = \frac{1}{2i}(\hat{S} - \hat{I}) \tag{2.17}$$

$$\hat{K} = i(\hat{I} - \hat{S})(\hat{I} + \hat{S})^{-1}, \tag{2.18}$$

where $\hat{I}$ is the identity matrix. I use all three of these. I compute the A and B amplitudes of the K-matrix formalism so that the work is formulated in terms of F_l and G_l. My phase shifts and mixing parameters are defined in the S-matrix formalism using Eq. (2.15). Scattering experiments involve incoming plane waves, so that the T-matrix is the natural framework to compute differential cross sections.

2.3 Near Threshold Scattering with Spin

For neutrons, precise measurements and nonresonant scattering has known energy dependence given by effective-range theory, so the limit that $k \to 0$ requires special attention from a theorist. I compute observables in this region by linearly extrapolating energy to lower values; experimentalists take many measurements at low energy for example with room-temperature or cooled neutrons, and theorists compute the limit for a given potential. For low-energy neutrons, the effective range expansion, of which the scattering length is a parameter is generally valid and helpful.

Some observables of interest in this limit are the total cross-section and the scattering length a, defined by

$$\lim_{k \to 0} \frac{k}{\tan \delta} = -\frac{1}{a}. \tag{2.19}$$

The standard interpretation of the scattering length is that the target scatters the projectile in the near-threshold limit as if it were a hard sphere of radius a. The total cross-section of that system is then similar to four times the classical result of a hard-sphere,

$$\lim_{k \to 0} \sigma = 4\pi a^2. \tag{2.20}$$

In the light nuclei with A=3 and 4, it is known that as one varies the potential, binding energies and scattering lengths vary in a correlated way that is referred to as the Phillips relation which relates triton binding energy to $n + d$ scattering lengths [46].

When there are multiple S-wave channels, each has its own scattering length and effective range. What is observed in measurements of total scattering depends on the scattering lengths in all channels and on the manner in which the target nuclei move independently or are bound in solid or molecular targets. For systems with two s-waves, such as $n + {}^3\text{H}$, the near-threshold observables are written as

$$\lim_{k\to 0} \sigma = \pi(a_0^2 + 3a_1^2), \tag{2.21}$$

and the coherent scattering length for spin-1/2 targets in diatomic molecules

$$\lim_{k\to 0} a = \frac{1}{4}(a_0 + 3a_1), \tag{2.22}$$

with,

$$a_s = \frac{\sin(\delta_s)}{k}, \tag{2.23}$$

and s labels spin. Here, I have taken the zero-energy limit of the total cross section for spin systems. We compute σ by integrating the spin-dependent differential cross-section:

$$\frac{d\sigma}{d\Omega} = \frac{1}{4}\text{Tr}\left(\mathbf{M}\mathbf{M}^\dagger\right), \tag{2.24}$$

over all angles. I introduce the scattering matrix, $\mathbf{M}$, and its components

$$M_{\mu\mu'}^{ss'}(\theta) = \frac{\sqrt{4\pi}}{k}\sum_{J=0}^{\infty}\sum_{ll'}\sqrt{2l+1}(l0s\mu|J\mu)(lm's'\mu'|J\mu)T_{ll'}^{ss'}Y_{l'm'}(\theta,0), \tag{2.25}$$

where $m = \mu - \mu'$ and $T_{ll'}^{ss'}$ is an element of the $\hat{T}$-matrix. This scattering matrix can be derived by explicitly following the spin dependence in the partial-wave expansion of Eq. (2.2), and it holds all the physical information from the L-coupling and S-coupling channels. For $n + {}^3\mathrm{H}$ in the zero-energy limit, it is convenient to compute and report it for the spin-zero and spin-one systems.

To obtain estimates at threshold, one traditionally performs a simple linear regression on the computed values of $k/\tan\delta$ approaching threshold to approximate the intercept, which is the negative inverse of the scattering length. In the case of thermal neutron scattering (1/40 eV), we can also evaluate observables near thermal energy and extrapolate.

Chapter 3

Quantum Monte Carlo

The QMC wave functions are approximate solutions of the nonrelativistic many-body Schrödinger equation,

$$\hat{H}\left|\Psi(\mathbf{R},J^{\pi},T,T_z)\right\rangle = E\left|\Psi(\mathbf{R},J^{\pi},T,T_z)\right\rangle, \tag{3.1}$$

with energy E, particle coordinates $\mathbf{R}=\{\mathbf{r}_1,\mathbf{r}_2,...,\mathbf{r}_{\mathrm{A}}\}$, total angular momentum J, parity π, total isospin T, isospin projection T_z, and Hamiltonian operator

$$\hat{H} = -\sum_{i=1}^{A}\frac{\hbar^2}{2m}\nabla_i^2 + \sum_{i<j}^{A} v_{ij} + \sum_{i<j<k}^{A} V_{ijk}. \tag{3.2}$$

Here sums run over particles, ∇_i^2 is the Laplacian operator in the coordinates of particle i, v_{ij} is the two-body potential between particles i and j, and V_{ijk} is the three-body potential among particles i, j, and k. The charge-conserving form of $|\Psi\rangle$ at each point in space is a $2^{\mathrm{A}} \times \binom{A}{Z}$ spin-isospin vector of complex amplitudes. However, in most systems and in this work isospin is a reasonably good quantum number. We can then reduce the total size of matrix operations on that vector using an isospin-conserving basis.

3.1 Variational Monte Carlo

In my calculations, I use variational wave functions of the form generally employed for nuclear VMC in bound systems [47–49], with minor modifications for scattering. Here, I describe the structure of the VMC wave functions, emphasizing aspects that require modification for scattering.

The variational wave function $|\Psi_V\rangle$ is constructed from two- and three-body operator correlations acting on a Jastrow wave function that contains only scalar correlations, assembled to have definite quantum numbers of angular momentum and isospin as well as antisymmetry under particle exchange [26]. The form of the variational ansatz used here is [50]

$$|\Psi_V\rangle = \left[\mathcal{S}\prod_{i<j}\left(1 + U_{ij} + \sum_{k\neq i,j} U_{ijk}\right)\right]|\Psi_J\rangle\,, \tag{3.3}$$

where the sums and products run over nucleon labels. The operator correlations contain the same operators on spin, isospin, and coordinates that appear in the largest terms of the nucleon-nucleon interaction. They have the forms

$$U_{ij} = \sum_{p=2,6}\left[\prod_{k\neq i,j} f^p_{ijk}(r_{ik}, r_{jk})\right] u_p(r_{ij}) O^p_{ij}, \tag{3.4}$$

where the indexed operators are $O_{ij}^{p=1,6} = [1, \boldsymbol{\sigma}_i \cdot \boldsymbol{\sigma}_j, S_{ij}] \otimes [1, \boldsymbol{\tau}_i \cdot \boldsymbol{\tau}_j]$. Here $\boldsymbol{\sigma}_i$, $\boldsymbol{\tau}_i$, and S_{ij} are spin, isospin, and spin-tensor operators, respectively, and r_{ij} is the distance between nucleons i and j. The spatial dependence $u_p(r_{ij})$ in each term is calculated from two-body Euler-Lagrange equations [51] that contain the nucleon-nucleon potential and variational parameters, while the correlations f^p_{ijk} suppress the spin-isospin pair correlations when a third particle is nearby. The three-body correlations U_{ijk} are constructed from operators appearing in three-body terms of the potential, but with strengths and pair-separation dependences scaled by variational parameters ϵ_p and b respectively,

$$U_{ijk} = -\sum_p \epsilon_p V^p_{ijk}(br_{ij}, br_{jk}, br_{ki}). \tag{3.5}$$

The operator $\mathcal{S}$ in Eq. (3.3) symmetrizes over orderings of the operators (which do not commute) so that $|\Psi_V\rangle$ inherits the antisymmetry of the Jastrow function.

For a given permutation of particle labels (that is, before antisymmetrization), each particle in the Jastrow function $|\Psi_J\rangle$ is assigned to the s- or the p-shell. The central pair correlations depend on this assignment, so, for example, $f_{ss}(r_{ij})$ is applied when particles i and j are both in the s-shell core described below, while $f_{sp}(r_{ij})$ is applied when one is in the s- and one in the p-shell. Then for a nucleus of A nucleons with a full four-particle s-shell and at least two p-shell particles (presented to connect this work to notation in the prior literature),

$$\begin{aligned} |\Psi_J\rangle \;=\; & \mathcal{A}\left\{ \prod_{i<j<k\leqslant 4} f^{sss}_{ijk} \prod_{t<u\leqslant 4} f^{ss}(r_{tu}) \prod_{i\leqslant 4}\ \prod_{5\leqslant j\leqslant A} f^{sp}(r_{ij}) \prod_{5\leqslant k<l\leqslant A} f^{pp}(r_{kl}) \right. \\ & \left. \times \sum_{LS[n]} \beta_{LS[n]} \left|\Phi_A(LS[n]JMTT_3)_P\right\rangle \right\}. \end{aligned} \tag{3.6}$$

If there is only one p-shell particle, then $f^{pp}_{ij} = 1$. The function

$$\begin{aligned} & \left|\Phi_A\left(LS[n]JMTT_3\right)_P\right\rangle \\ & = \left| \Phi_\alpha(0000)_{1234} \prod_{5\leqslant i\leqslant A} \phi_p^{LS[n]}(r_{\alpha i}) \right. \\ & \times \left[\left[\prod_{5\leqslant j\leqslant A} Y_{lm_l}\left(\hat{\mathbf{r}}_{\alpha j}\right) \right]_{LM_L} \otimes \left[\prod_{5\leqslant k\leqslant A} \chi_k\left(\frac{1}{2}m_i\right) \right]_{SM_S} \right]_{JM} \\ & \times \left. \left[\prod_{5\leqslant l\leqslant A} \nu_i\left(\frac{1}{2}t_z\right) \right]_{TT_z} \right\rangle, \end{aligned} \tag{3.7}$$

is a spin-isospin vector that depends on the partition of the particles, in which the first four nucleons are assigned to the s-shell (or "alpha core"). This core is constructed as a simple Slater determinant of spins and isospins coupled to definite total angular momentum and isospin quantum numbers denoted by $\Phi_\alpha(J{=}0, M{=}0, T{=}0, T_z{=}0)_{1234}$, while the remaining particles are assigned to p-shell orbitals. Spinors χ_i and ν_i specify spin and isospin states of the p-shell particles, and spherical harmonics Y_{lm_l} describe their angular motion around the center of mass of the core, from which they are separated by vectors $\mathbf{r}_{\alpha i}$. These are coupled to specified quantum numbers of total spin S, orbital angular momentum L and net angular momentum J (with projection M), as well as total isospin T (with projection T_z), as indicated by square brackets. Full specification in general also requires a definite permutation symmetry among p-shell orbitals, in the form of a Young diagram label $[n]$.

Each p-shell orbital $\phi_p^{LS[n]}(r_{\alpha i})$ depends on the magnitude of $\mathbf{r}_{\alpha i}$ (keeping the wave function translation-invariant), and on the specified quantum numbers. Since pair correlations appear elsewhere, $\phi_p^{LS[n]}$ can be thought of as accounting for interactions with the mean field of the nucleus, and as allowing antisymmetry when $A > 4$. The f_{sp} are constructed explicitly to describe close-in-pair correlations, so that $f_{sp}(r \to \infty) = 1$, and the exponential drop-off of the wave function at large $r_{\alpha i}$ for bound states is built into $\phi_p^{LS[n]}$. Each $\phi_p^{LS[n]}(r_{\alpha i})$ is accordingly computed from a Woods-Saxon potential well with orbital angular momentum $l = 1$ (for a p-shell nucleus) in a one-body Schrödinger equation. The geometric parameters of the wells and their separation energies are parameters to be varied in the VMC procedure, with the initial guess of the separation energy given by the appropriate breakup threshold for the nuclear system at hand. Configurations having all the quantum numbers L, S, and $[n]$ that can be consistent with the given J, T, and T_z are generally present, so they are all included with weight amplitudes $\beta_{LS[n]}$ in Eq. (3.6). Finally, the operator $\mathcal{A}$ denotes an antisymmetric sum over every permutation P of particle labels.

All of the correlations and orbitals are either explicit functions of variational parameters or solutions of differential equations whose constants are treated as variational parameters.

Optimal values of all parameters are found from a Rayleigh-Ritz variational principle by minimizing the energy expectation value

$$E_V = \frac{\langle \Psi_V | \hat{H} | \Psi_V \rangle}{\langle \Psi_V | \Psi_V \rangle}. \tag{3.8}$$

The integrals in Eq. (3.8) and other matrix elements are calculated by Monte Carlo integration, using $\Psi_V^\dagger \Psi_V$ (a function of particle coordinates) as weight function. I optimize parameters using an implementation of the nonlinear optimizing algorithm COBYLA from the NLopt library [52]. After minimization, the result of VMC is a variational upper bound on the energy expectation value and an optimized wave function that can be used as an input to further calculations.

3.1.1 VMC Scattering States

This general framework is adaptable to unbound states [25, 29, 30]. The eigenvalue nature of bound states arises from the condition that their wave functions should be square-integrable. This is enforced in VMC by exponential decay at large distances in the f_{ss} correlations and in the p-shell orbitals $\phi_p^{LS[n]}$. Scattering formally involves wave functions that extend to infinity and cannot be found by energy minimization. However, we can adapt the VMC procedure and wave function to scattering by confining the wave function to a spherical box and imposing a boundary condition at its edge. The boundary condition renders the kinetic energy operator Hermitian and the wave function normalizable, so that VMC energy minimization gives access to a unique ground state. Once this ground state has been found, it may be smoothly matched onto asymptotic scattering solutions outside the box and viewed as the portion of a scattering wave function near the origin.

The most useful boundary condition for single-channel scattering is a specified logarithmic derivative ζ_c of the wave function at the box surface, defined by

$$\hat{\mathbf{n}}_c \cdot \nabla_{\mathbf{r}_c}\big(\mathbf{r}_c\,|\Psi\rangle\,\big) = \zeta_c \mathbf{r}_c\,|\Psi\rangle\,, \tag{3.9}$$

where the subscript c denotes a scattering channel specified by a division of nucleons into two nuclei and by values of J, M_J, L, and S. The gradient is evaluated in coordinates defined by the vector $\mathbf{r}_c$ that separates the centers of mass of the scattering nuclei and $\hat{\mathbf{n}}_{\mathbf{c}}$ is an outward normal unit vector at the surface of the box, defined by $r_c = R_0$ for a box of radius R_0. For fixed R_0, different choices of ζ_c give boxes with different ground state energies, corresponding to scattering at different energies.

The wave function ansatz of Eqs. (3.3)–(3.7) is easily adapted to describe the scattering of a single nucleon by an s-shell nucleus. The s-shell nucleus is well-described by a spin-isospin Slater determinant and correlations between its nucleons, just like the s-shell portion of Eqs. (3.3) and (3.6) [53]. The scattered nucleon can be incorporated into the wave function just like the p-shell particles in Eq. (3.7), using the same routines in the VMC code but narrowing to the case of only one "p-shell" particle, which could have any value of $L = l$ for its orbital motion around the nuclear center of mass, not just $l = 1$. Then the coordinate $\mathbf{r}_{\alpha j}$ in Eq. (3.7) is identical to the channel separation $\mathbf{r}_c$ for scattering. For scattering from a triton, the Slater determinant for the core contains only three particles, coupled to $J = 1/2$, $T = 1/2$, $T_z = -1/2$ to form $\Phi_t(\frac{1}{2}\frac{1}{2}\frac{1}{2}(-\frac{1}{2}))_{123}$; the correlations ss and sss should in principle be optimized for the triton ground state so that configurations at the box surface truly match onto a triton cluster outside the box. To produce a specific scattering channel with good quantum numbers, the angular momentum coupling in Eq. (3.7) has to be adapted to couple the scattered nucleons to the $J = 1/2$ core. Fermionic exchange of the scattered nucleon with a nucleon of the core enters through the antisymmetrization in Eq. (3.6). A similar but more elaborate approach has been used for scattering of composite nuclei and for highly clustered nuclei, when one of the clusters is an alpha particle [54–56].

Since the sp pair correlations are constrained to go over to the identity operator at large separation, placement of R_0 at large enough radius turns Eq. (3.9) into a boundary condition on computation of $u_c = r_c \phi_p^{LS[n]}$ from its Woods-Saxon well, so that in principle

$$\zeta_c u_c(R_0) = \left.\frac{du_c}{dr_c}\right|_{r_c=R_0} . \tag{3.10}$$

However, in optimizing the wave function it is often possible to lower E_V by altering the cutoff parameter that enforces $f_{sp} \longrightarrow 1$ at large separations, as assumed in using Eq. (3.10) as a boundary condition on the whole wave function. When the cutoff radius becomes too large, the f_{sp} correlations gain a slope near the box surface and alter ζ_c. To solve this problem, I apply the condition in Eq. (3.10) to the product $[f_{sp}(r_c)]^{n_{sp}} u_c(r_c)$ instead of just $u_c(r_c)$ by itself, where n_{sp} is the number of nucleons in the scattering nucleus ($n_{sp} = 3$ for $n + {}^3\mathrm{H}$). This works because high-probability configurations all have a distance from a neutron at the box boundary to any nucleon inside the triton or alpha particle (mean radius 1.7 and 1.68 fm, respectively, smaller than my 9 fm box) close to r_c on average. I found that the modified Eq. (3.10) enforces the desired boundary condition in Eq. (3.9) on the wave function with good precision. It also prevents the optimizer from pushing the f_{sp} cutoff to larger radius, removing a significant source of difficulty in the variational search.

For coupled-channels problems there is a ζ_c for each channel and also a β_c amplitude (corresponding to the $\beta_{LS[n]}$ of a bound state), but I leave that complication for later sections. The value of ζ_c in a single uncoupled channel (so that no β_c is needed) determines the energy of the lowest state in the box, which I find by the usual energy minimization. Repeated calculations at many different ζ_c values yield scattering wave functions over a range of energies. At each energy, the values of ζ_c and β_c determine how the wave function matches across the box boundary, yielding phase shifts and mixing parameters (and therefore observables) as functions of energy.

3.2 Green's function Monte Carlo

Green's function Monte Carlo (GFMC) is a method for projecting out properties of the true ground state wave function from an initial variational solution. In my GFMC work, I use the same code base described in Ref. [57], which was originally developed and presented in Ref. [48, 58]. Starting from VMC wave functions, we apply the imaginary-time evolution operator,

$$\lim_{\tau \to \infty} e^{-(H' - E_{\rm g})\tau}, \tag{3.11}$$

where $\tau = it$, $E_{\rm g}$ is a guess for the ground state energy, and H' is a local (diagonal in position space) approximation to the full Hamiltonian. In practice, we can only compute the propagator accurately for sufficiently small changes in τ ($\Delta\tau < 0.1$ GeV^{-1}). Evolution to large imaginary time τ is then carried out by repeated propagation at small $\Delta\tau$ steps, where the propagated wave function,

$$\Psi(\tau) = \left[e^{-(H' - E_{\rm g})\Delta\tau} \right]^{N_\tau} \Psi_V, \tag{3.12}$$

obviously $\Psi(0) = \Psi_V$, and the evolution to τ involves $N_\tau = \tau/\Delta\tau$ total steps. We evaluate the precomputed short-time propagator as a Green's function, $G_{\alpha\beta}(\mathbf{R}', \mathbf{R}; \Delta\tau)$, which propagates a spin-isospin vector at location $\mathbf{R}$ in configuration space into a new spin-isospin vector at location $\mathbf{R}'$. Locations $\mathbf{R}$ are specified by the coordinates of all particles. Since G takes a vector to a vector, it is a matrix operator and is defined as

$$G_{\alpha,\beta}(\mathbf{R}', \mathbf{R}; \Delta\tau) = \langle \mathbf{R}', \alpha | \, e^{-(H' - E_{\rm g})\Delta\tau} \, | \mathbf{R}, \beta \rangle \,, \tag{3.13}$$

where α and β indicate spin-isospin indices and for compactness will be hidden in later equations. $\mathbf{R}'$ is the new position of particles, chosen by following a rejection sampling algorithm [26] for reasons described below. Having computed the short-time propagator, we can begin to build up our wave function to large τ, where the final propagation step will be

$$\Psi_{N_\tau}(\mathbf{R}_{N_\tau}) = \int G(\mathbf{R}_{N_\tau}, \mathbf{R}_{N_\tau-1}; \Delta\tau)\Psi_{N_\tau-1}(\mathbf{R}_{N_\tau-1})d\mathbf{R}_{N_\tau-1}. \tag{3.14}$$

We can then immediately start to unroll the entire propagation into many repeated integrals, which can be sampled using a Monte Carlo Markov chain,

$$\Psi_{N_\tau}(\mathbf{R}_{N_\tau}) = \int \prod_{n=0}^{N_\tau-1} \left\{G(\mathbf{R}_{n+1}, \mathbf{R}_n; \Delta\tau)\right\} \cdot \Psi_V(\mathbf{R}_0) \prod_{n=0}^{N_\tau-1} d\mathbf{R}_n. \tag{3.15}$$

This brings us back to the initial VMC wave function; GFMC starts with a swarm of samples from Ψ_V, and each of those becomes a “walker”. Each walker follows its own Markov chain path through configuration space from one τ value to the next. The combination of Green’s functions and Monte Carlo integration is where GFMC gets its name. A single walker contributes to a single energy evaluation, but on the order of 10^5 initial configurations are generated in a practical calculation to provide good statistics. In order to guarantee that the calculation does not become dominated by a few walkers, a branching algorithm either multiplies or kills walkers based on their projected growth. The walkers also follow an importance sampling distribution based on $\Psi^\dagger(\mathbf{R};\tau)\Psi_V(\mathbf{R})$ (an inner product in the spin-isospin space) at each propagated point. After a set number of propagation steps (∼20-80), we compute the energy expectation value at the corresponding τ. After propagating to large enough τ, the averaged energy in a successful calculation stabilizes to the ground state energy with some sampling noise.

Unfortunately, during propagation of the wave function, the variance of the computed energy begins to grow exponentially unless some countermeasure is taken, a difficulty known as the fermion sign problem. This difficulty arises because there is an unphysical bosonic ground state with (much) lower energy than the fermionic ground state. Sampling individual points provides no way to enforce a nonlocal constraint like antisymmetry under particle exchange.

The contribution of the bosonic state to the walkers grows, and when energy is evaluated by projecting this mostly bosonic state onto the antisymmetric variational wave function (as described below), the result is eventually numerical noise with no signal. The GFMC code solves this problem with a constrained path algorithm [59, 60] that requires each walker to have a positive overlap at each step with the variational starting point,

$$\Psi^{\dagger}(\mathbf{R};\tau)\Psi_V(\mathbf{R}) > 0. \tag{3.16}$$

Like the fixed-node approximation used to solve the sign problem in many-electron systems, this approximation is limited by the quality of the variational wave function. Fortunately, nuclear VMC is an excellent starting point in its own right. However, the constrained path can cause convergence to the wrong energy (lower or higher). To alleviate this problem, we release the constraint for several steps to reduce these errors before each energy calculation. The number of unconstrained steps is usually 10-30 for bound states [26]. and for unbound states of ^{5}He, it has been found that around 80 steps are necessary to avoid introducing a bias of 10-20 keV in energy evaluation [25]. We can also store all of the spin-isospin vectors from the energy calculations for later offline calculations of other quantities.

Expectation values based on a propagated GFMC wave function, in principle, only require that wave function and the desired operator $\mathcal{O}$,

$$\langle\mathcal{O}\rangle = \langle\Psi(\tau)|\,\mathcal{O}\,|\Psi(\tau)\rangle\,. \tag{3.17}$$

If the operator $\mathcal{O}$ contains derivatives, we face the problem that GFMC only gives us amplitudes at discreet points in space, and computation of the derivatives in Eq. (3.17) is impossible. Additionally there is a mismatch between sample locations on the left and right propagated wave functions. Nonetheless, we can write $\Psi(\tau) = \Psi_V + \delta\Psi(\tau)$, where $\delta\Psi(\tau)$ is small and terms of order $[\delta\Psi(\tau)]^2$ are assumed negligible, and obtain the commonly used approximation [57, 60–62],

$$\langle \mathcal{O} \rangle \approx \langle \mathcal{O} \rangle_L + \langle \mathcal{O} \rangle_R - \langle \mathcal{O} \rangle_V . \tag{3.18}$$

Here subscript V denotes the variational expectation value,

$$\langle \mathcal{O} \rangle_V = \langle \Psi_V | \, \mathcal{O} \, | \Psi_V \rangle , \tag{3.19}$$

with L (left) and R (right) denoting which side the propagator acts on:

$$\langle \mathcal{O} \rangle_L = \langle \Psi(\tau) | \, \mathcal{O} \, | \Psi_V \rangle \tag{3.20}$$

$$\langle \mathcal{O} \rangle_R = \langle \Psi_V | \, \mathcal{O} \, | \Psi(\tau) \rangle . \tag{3.21}$$

In most cases, $\langle \mathcal{O} \rangle_{\mathrm{L}}$ and $\langle \mathcal{O} \rangle_{\mathrm{R}}$ evaluate to nearly the same value; they are called "mixed estimates". The energy is a special case in computing expectation values, as the Hamiltonian commutes with the propagator. We see why this is important by splitting the propagation in half and commuting the Hamiltonian past the short-time propagators for one half of the evolution,

$$E = \langle \Psi_V | \, \hat{H} \, | \Psi(\tau) \rangle = \langle \Psi(\tau/2) | \, \hat{H} \, | \Psi(\tau/2) \rangle . \tag{3.22}$$

For sufficiently large τ, Eq. 3.22 will approach $E_{g.s.}$. Additionally, recall that in practice, we use a localized approximation to the Hamiltonian (H'). We compute $\langle \hat{H} - H' \rangle$ perturbatively via Eq. (3.18) to remedy this.

In this work, I have a more complicated mixed estimate to evaluate for the integral method amplitudes (an off-diagonal case), because I have a channel cluster product function on the left and an A-body scattering wave function on the right. Therefore, evaluating the left and right matrix elements, analogous to the left and right expectation values above, requires similar but different computations. Following the derivations in Refs. [41, 61] and labeling the initial and final nuclear states in those matrix element calculations as Ψ^i and Ψ^f respectively, we can obtain the general formulation for GFMC mixed estimates of off-diagonal quantities,

$$\frac{\langle \Psi^f(\tau)| \, \mathcal{O} \, |\Psi^i(\tau)\rangle}{\sqrt{\langle \Psi^f(\tau)|\Psi^f(\tau)\rangle}\sqrt{\langle \Psi^i(\tau)|\Psi^f(\tau)\rangle}} \approx \langle \mathcal{O}(\tau)\rangle_{M_i} + \langle \mathcal{O}(\tau)\rangle_{M_f} - \langle \mathcal{O}\rangle_V \,, \tag{3.23}$$

where

$$\langle \mathcal{O}\rangle_V = \frac{\langle \Psi_V^f| \, \mathcal{O} \, |\Psi_V^i\rangle}{\sqrt{\langle \Psi_V^f|\Psi_V^f\rangle}\sqrt{\langle \Psi_V^i|\Psi_V^i\rangle}}, \tag{3.24}$$

$$\langle \mathcal{O}(\tau)\rangle_{M_i} = \frac{\langle \Psi_V^f| \, \mathcal{O} \, |\Psi^i(\tau)\rangle}{\langle \Psi_V^i|\Psi^i(\tau)\rangle}\sqrt{\frac{\langle \Psi_V^i|\Psi_V^i\rangle}{\langle \Psi_V^f|\Psi_V^f\rangle}}, \tag{3.25}$$

and

$$\langle \mathcal{O}(\tau)\rangle_{M_f} = \frac{\langle \Psi^f(\tau)| \, \mathcal{O} \, |\Psi_V^i\rangle}{\langle \Psi^f(\tau)|\Psi_V^f\rangle}\sqrt{\frac{\langle \Psi_V^f|\Psi_V^f\rangle}{\langle \Psi_V^i|\Psi_V^i\rangle}}. \tag{3.26}$$

As I do not have an initial and final state in this work, I refer to mixed estimates in later sections as involving "right" and "left" states instead of "initial" and "final" states, and my notation below reflects those terms. Since derivative operators can only act on Ψ_V but the codebase always places cluster-product functions on the left, significant code development was needed to set up action of the potential operator toward the left in Eq. (3.25).

3.2.1 GFMC Scattering States

We build GFMC scattering wave functions from the same particle in-a-box framework as the VMC case. Because GFMC operates only on isolated points in configuration space, the logarithmic derivative boundary condition cannot be explicitly enforced. However, the equivalence of the particle-in-a-box wave function to the short-range part of a wave function filling all of space provides a way to incorporate the boundary condition [25, 63]. GFMC walkers would cross the boundary in both directions if the entire wave function were present, and the wave function inside the box would contain contributions propagated from within and from outside. At each propagation step, the integral in Eq. (3.14) is then split into contributions from inside and outside the box,

$$\Psi_{n+1}(\mathbf{R}') = \int_{|\mathbf{r}_{12}|<R_0} G(\mathbf{R}', \mathbf{R}_n; \Delta\tau)\Psi_n(\mathbf{R}_n) d\mathbf{R}_1 d\mathbf{R}_2 d\mathbf{r}_{12} + \int_{|\mathbf{r}_{12}|>R_0} G(\mathbf{R}', \mathbf{R}_n; \Delta\tau)\Psi_n(\mathbf{R}_n) d\mathbf{R}_1 d\mathbf{R}_2 d\mathbf{r}_{>}, \tag{3.27}$$

where $\mathbf{R}_1$ and $\mathbf{R}_2$ represent the internal cluster coordinates inside the clusters, $\mathbf{r}_{12}$ is the separation of cluster centers of mass inside the box; $\mathbf{r}_{>}$ is the separation of cluster centers of mass when $|\mathbf{r}_{12}| > \mathrm{R}_0$ [25, 63]. We can then map every point in the second integral into a point in the first integral with the change of variable $\mathbf{r}_{>} = (r_{>}/\mathrm{R}_0)^2\mathbf{r_{12}}$. This substitution maps the outside integral into the box,

$$\Psi_{n+1}(\mathbf{R}') = \int_{|\mathbf{r}_{12}|<R_0} G(\mathbf{R}', \mathbf{R}_n; \Delta\tau)\Psi_n(\mathbf{R}_n) d\mathbf{R}_1 d\mathbf{R}_2 d\mathbf{r}_{12} + \int_{|\mathbf{r}_{12}|<R_0} G(\mathbf{R}', \mathbf{R}_{>}; \Delta\tau)\left(\frac{r_{>}}{r}\right)^3 \Psi_n(\mathbf{R}_{>}) d\mathbf{R}_1 d\mathbf{R}_2 d\mathbf{r}_{12}, \tag{3.28}$$

where $\mathbf{R}_{>}$ is the "image" location outside the box implied by the value of $\mathbf{r}_{>}$. However, we do not sample the wave function outside the box, so $\Psi(\mathbf{R}_{>})$ is not directly available. Fortunately, because $G(\mathbf{R}', \mathbf{R}, \Delta\tau)$ is evaluated for small $\Delta\tau$, the propagator range is small. The short range implies that only when we are "near" ($|\mathbf{r} - \mathbf{r}_{>}| \leqslant 1$ fm) the surface of the box will these contributions become significant during a single time step. Thus a simple linear extrapolation to compute $\Psi(\mathbf{R}_{>})$ will suffice,

$$\Psi_n(\mathbf{R}_{>}) \approx (1 + \zeta_c(\mathbf{R}_{>} - \mathbf{R})\cdot\hat{\mathbf{n}})\Psi_n(\mathbf{R}), \tag{3.29}$$

where ζ_c is the same boundary condition from the VMC wave function and $\hat{\mathbf{n}}$ is the outward direction perpendicular to the box surface. The propagated wave function for scattering states is then

$$\Psi_{n+1}(\mathbf{R}') = \int_{|\mathbf{r}_{12}|<R_0} \left(G(\mathbf{R}', \mathbf{R}_n) + G(\mathbf{R}', \mathbf{R}_>)[1 + \zeta_c(\mathbf{R}_> - \mathbf{R}_n) \cdot \hat{\mathbf{n}}] \left(\frac{r_>}{r}\right)^3 \right) \Psi_n(\mathbf{R}_n) d\mathbf{R}_n. \tag{3.30}$$

From there, we carry out the GFMC algorithm as usual. This specific method has been successfully applied to n-alpha scattering in Refs. [25, 31]

Chapter 4

Determination of Overlaps and Scattering Observables

Here I describe the direct and integral methods for computing spectroscopic overlaps and scattering observables, including details for both VMC and GFMC wave functions.

4.1 Direct Method

Let us first examine the connection of particle-in-a-box wave functions to scattering phase shifts. Applying Eqs. (2.9), (3.9) and (2.15) at the boundary of radius R_0 (and omitting the channel label c) one finds $B/A = \tan\delta$ for single-channel scattering. It then follows from Eqs. (3.9) and (2.9) that B/A is equal to

$$\tan\delta = \left.\frac{k\frac{\partial}{\partial\rho}F_l(\eta,\rho) - \zeta F_l(\eta,\rho)}{\zeta G_l(\eta,\rho) - k\frac{\partial}{\partial\rho}G_l(\eta,\rho)}\right|_{\rho=kR_0}. \tag{4.1}$$

Here, we have the phase shift as an explicit function of ζ and the channel energy (which enters through η and k), without the need to compute A or B if the energy is accurately computed. Choosing a value of ζ, we calculate the corresponding energy, subtract the threshold energy to obtain the channel energy, and compute the phase shift from Eq. (4.1). Repetition at several ζ values maps out δ as a function of energy. When there are coupled channels, the linear relationship among amplitudes is more complicated than a simple ratio, and one of Eqs. (2.12), (2.13), or (2.14) has to be inverted. When computing a wave function for that case, both the amplitudes (by setting $\beta_{LS[n]}$ parameters in Eq. (3.6)) and the ζ_c values are inputs. Inversion of Eq. (2.12) to obtain $\hat{K}$ requires two or more (depending on the number of channels) linearly independent solutions constructed to have the same or nearly the same energy.

The amplitudes described by the scattering matrices are effectively values of spectroscopic overlap functions, computed by projection of a state onto the cluster-product function of Eq. (2.8). A spectroscopic overlap onto a scattering channel is defined as

$$R_c(r) = \frac{1}{\mathcal{N}_V} \langle \Psi^c_{1\otimes 2} | \frac{\delta(r - r_c)}{r_c^2} | \Psi_V \rangle \,, \tag{4.2}$$

where

$$\mathcal{N}_V \equiv \sqrt{\langle \psi^{J_{1c}}_{1c} | \psi^{J_{1c}}_{1c} \rangle \langle \Psi_V | \Psi_V \rangle} \tag{4.3}$$

normalizes the wave functions (cluster 2 being only a neutron spinor in the neutron scattering cases examined in this work). In principle, the cluster product function is antisymmetrized with respect to nucleon exchange between clusters, as in Eq. (2.8). However, the explicit antisymmetry of $|\Psi_V\rangle$ has the result that an antisymmetrized $|\Psi^c_{1\otimes 2}\rangle$ gives the same $R_c(r)$ as a single permutation, multiplied by the square root of the number of possible exchanges (A exchanges for scattering of a nucleon from an (A-1)-body nucleus.); therefore, we use a single permutation and replace the operator $\mathcal{A}_c$ by the appropriate multiplicative factor. Finally, all of our wave functions are explicitly translation invariant, so no correction factor is needed to account for use of fixed-center basis states.

The spectroscopic factor is defined as the norm of the overlap,

$$S_c = \int_0^\infty |R_c(r)|^2 \, r^2 dr. \tag{4.4}$$

My definition of this norm is consistent with previous QMC works [41, 64] and similar calculations [36] but differs from some [65, 66] by inclusion of Clebsch-Gordan coefficients into the cluster product function. Although I do not present any results of spectroscopic factors in this work, it is worth describing their calculation due to similarities in the calculation between spectroscopic factors and surface amplitudes (A,B). In principle, the A_c and B_c amplitudes could be read from our wave function specification using values of β_c, $\phi_c(R_0)$, and ζ_c. Instead, to directly determine asymptotic amplitudes, I examine the overlap in each channel and separate it into terms F_l and G_l at the surface of the box. As I show below, overlap functions near the center of the box are also useful for interpretation and validation of the integral method, particularly since the computational routines for one-nucleon removal overlaps have a long history of previous use [41, 67].

Evaluation of the overlap integral in VMC is straightforward with the same techniques used in energy expectation values. To compute spectroscopic overlaps (and spectroscopic factors) using GFMC wave functions, we need to evaluate Eq. (3.23) with $\mathcal{O} = \delta(r - r_c)/r_c^2$ as in Ref. [41]. Applying the general Eq. (3.23) to the specfic case of Eq. (4.2), we find the resulting GFMC spectroscopic overlap,

$$\begin{aligned} R_c(r) \approx &- \frac{1}{\mathcal{N}_V} \langle \Psi^c_{1\otimes 2}(\tau = 0)| \frac{\delta(r - r_c)}{r_c^2} |\Psi_V\rangle \\ &+ \frac{1}{\mathcal{N}_L} \langle \Psi^c_{1\otimes 2}(\tau)| \frac{\delta(r - r_c)}{r_c^2} |\Psi_V\rangle \\ &+ \frac{1}{\mathcal{N}_R} \langle \Psi^c_{1\otimes 2}(\tau = 0)| \frac{\delta(r - r_c)}{r_c^2} |\Psi(\tau)\rangle \, , \end{aligned} \tag{4.5}$$

with the left norm

$$\mathcal{N}_L \equiv \sqrt{\mathcal{N}}\,\langle\psi_{1c}^{J_{1c}}(\tau)|\psi_{1c}^{J_{1c}}(\tau=0)\rangle\,, \tag{4.6}$$

and the right norm

$$\mathcal{N}_R \equiv \sqrt{\frac{1}{\mathcal{N}}}\,\langle\Psi_V|\Psi(\tau)\rangle\,, \tag{4.7}$$

where the self normalization factor

$$\mathcal{N} \equiv \frac{\langle\Psi_V|\Psi_V\rangle}{\langle\psi_{1c}^{J_{1c}}(0)|\psi_{1c}^{J_{1c}}(0)\rangle}. \tag{4.8}$$

I have also introduced the GFMC cluster-product function

$$\Psi^c_{1\otimes 2}(\tau) = \mathcal{A}_c\left[\psi_{1c}^{J_{1c}}(\tau)\otimes\left[\psi_{2c}^{J_{2c}}\otimes Y_{l_c}(\hat{r}_c)\right]_{j_c}\right]_J\,, \tag{4.9}$$

which is nearly the same as Eq. (2.8) but with the GFMC-propagated "core" wave function, $\psi_{1c}^{J_{1c}}(\tau)$; when $\tau = 0$ they are equivalent.

These off-diagonal calculations are carried out in the VMC code using stored GFMC samples, just as in off-diagonal calculations in Refs. [41, 61]. When the GFMC-evolved wave function is the full A-body function on the right, the locations of the GFMC samples define sampling for all A particles. When the GFMC-evolved function is the $(A-1)$-body target or core on the left, the GFMC samples only give locations for those $A-1$ particles. A choice then has to be made for how to sample locations of the projectile or valence particle. We must then assign a probability distribution $\rho(r_c)$ for the cluster separation (r_c) in this case. In principle, any distribution will suffice. However, the Monte Carlo statistical variance depends on the choice. As long as $\left|\psi_{1c}^{J_{1c}}\cdot\rho(r_c)\right|^2$ is a reasonable approximation of the A-body wave function sampling density, the variance of $\mathcal{N}$ will be acceptable. To preserve $\mathcal{N}$, we require that $\int_{r_c<R_0}\rho^2(r_c)dr_c = 1$. For bound states, either a Gaussian or a Woods-Saxon function works well for $\rho(r_c)$ [41]. However, for scattering calculations, I have found that an exponential

decay function,

$$\rho(r_c) = \sqrt{2}e^{-a_\rho r_c}, \tag{4.10}$$

diminishes sampling variances in the outer regions of the 9 fm box by an appropriate amount when $a_\rho = 1\ \mathrm{fm}^{-1}$.

4.2 Integral Method

Alternatively, the surface amplitudes may be computed from integrals over the part of the box interior where all of the nucleons interact. I start with the K-matrix formalism, defined by the standing wave in Eq. (2.9). Application of Green's theorem over a sphere of fixed cluster separation r_c, together with the Wronskian relation for the Coulomb functions at the sphere's surface, gives

$$\frac{2\mu k_c}{\hbar^2}\left(\langle \mathcal{F}_c|\,\hat{H} - E\,|\mathcal{G}_c\rangle - \langle \mathcal{G}_c|\,\hat{H} - E\,|\mathcal{F}_c\rangle\right) = 1, \tag{4.11}$$

where H is the full many-body Hamiltonian and E is the total energy. The Dirac bracket here denotes full contraction of the spin-isospin vector at every point and integration over all independent nucleon coordinates in the center-of-mass frame. This expression is nonzero because the Laplacian operator inside H is not Hermitian in a finite region (without further specification of a boundary condition) [23, 40].

If the sphere of constant r_c is located where the limit in Eq. (2.9) holds, we obtain from Eq. (4.11)

$$A_c = \frac{2\mu k_c}{\hbar^2}\left(\langle \Psi|\,\hat{H} - E\,|\mathcal{G}_c\rangle - \langle \mathcal{G}_c|\,\hat{H} - E\,|\Psi\rangle\right) \tag{4.12}$$

and

$$B_c = \frac{2\mu k_c}{\hbar^2}\left(\langle \mathcal{F}_c|\,\hat{H} - E\,|\Psi\rangle - \langle \Psi|\,\hat{H} - E\,|\mathcal{F}_c\rangle\right). \tag{4.13}$$

Applying the condition that $(\hat{H} - E)\,|\Psi\rangle = 0$ to the surface amplitudes of Eqs. (4.12) and (4.13) gives

$$A_c = \frac{2\mu k_c}{\hbar^2} \langle\Psi|\, \hat{H} - E \,|\mathcal{G}_c\rangle \tag{4.14}$$

and

$$B_c = -\frac{2\mu k_c}{\hbar^2} \langle\Psi|\, \hat{H} - E \,|\mathcal{F}_c\rangle\,. \tag{4.15}$$

The main difficulty in evaluating these expressions lies in Eq. (4.14), where the divergence in G_l at $r_c = 0$ gives rise to a delta function in the $\nabla^2 G_l$ term of the integrand. I resolve this difficulty using the regularization strategy described in Refs. [4, 23, 24, 40]. The essential property of G_l for application of Eqs. (4.11)-(4.15) is that it satisfies a Wronskian relation with F_l outside the interaction region. Any function satisfying that relation at the $r_c = R_0$ box boundary would work just as well, so I replace $\mathcal{G}_c$ with a regularized function $\widetilde{\mathcal{G}}_c$ that has the properties

$$\widetilde{\mathcal{G}}_c = f^c_{\text{reg}} \mathcal{G}_c \tag{4.16}$$

$$\widetilde{\mathcal{G}}_c(r_c \to 0) = 0 \tag{4.17}$$

$$\widetilde{\mathcal{G}}_c(r_c \to R_0) = \mathcal{G}_c. \tag{4.18}$$

One possible choice of the regularizer that satisfies these properties for all partial waves and eliminates the delta function is

$$f^c_{\text{reg}}(\gamma, r) = (1 - e^{-\gamma r})^{2l+1}, \tag{4.19}$$

where γ is a parameter to be fixed. I tried a few different regularizing functions, but this one produced the best evidence of giving correct results when γ is chosen within a favorable range (as shown below). This specific regularizer has been used in hyperspherical harmonic calculations in recent years [23, 24, 40, 68]. Here, I explore its application in the QMC context.

Starting from Eq. (4.11) and replacing G_l with $\tilde{G}_l$ we find similar results as before, with initially

$$\frac{2\mu k_c}{\hbar^2}(\langle\mathcal{F}_c|\,\hat{H}-E\,|\widetilde{\mathcal{G}}_c\rangle-\langle\widetilde{\mathcal{G}}_c|\,\hat{H}-E\,|\mathcal{F}_c\rangle)=1. \tag{4.20}$$

Picking up from there, Eq. (4.15) for B_c remains the same. However, A_c of Eq.(4.14) becomes

$$A_c=\frac{2\mu k_c}{\hbar^2}\,\langle\Psi|\,\hat{H}-E\,|\widetilde{\mathcal{G}}_c\rangle\,. \tag{4.21}$$

Further simplification follows from a separation of the Hamiltonian into three parts, $H{=}H_{\mathrm{rel}}{+}H_1+H_2$, suggested by partitioning the nucleons of $\tilde{\mathcal{G}}_l$ into clusters ψ_{c1} and ψ_{c2}. Parts H_1 and H_2 contain only the relative coordinates and spinors inside ψ_{c1} and ψ_{c2}, respectively. The third part H_{rel} contains the kinetic energy of cluster relative motion and all terms of the nucleon-nucleon potential that act between nucleons that are not in the same cluster [38]. I denote this sum of different cluster potential terms in channel c as V^c_{rel} (which depends on how nucleons are partitioned). I similarly divide the energy into $E = E_c + E_1 + E_2$, where E_c is energy relative to the threshold of channel c, while $(H_1 - E_1)\psi_{c1} = 0$ and $(H_2 - E_2)\psi_{c2} = 0$. For exact solutions, the terms H_1 and H_2 then cancel out of Eqs. (4.15) and (4.21). Furthermore, the point Coulomb potential $V^c_{\mathcal{C}} \equiv Z_1Z_2e^2/r_c$ can be added and subtracted from H to take advantage of the appearance of that term in Eq. (2.5) defining the Coulomb functions.

After that work and after applying the Laplacian operator in H_{rel} to the function $f^c_{\mathrm{reg}}(r)$ inside $\widetilde{\mathcal{G}}_c = f^c_{\mathrm{reg}}\mathcal{G}_c$, the integrals of Eqs. (4.15) and (4.21) become

$$B_c=-\frac{2\mu}{\hbar^2}\int_0^\infty \Psi^\dagger(\hat{V}^c_{\mathrm{rel}}-V^c_{\mathcal{C}})\mathcal{F}_c\,d^{3A}R \tag{4.22}$$

and

$$A_c = \int_0^\infty \Psi^\dagger \left\{ \frac{2\mu}{\hbar^2}(\hat{V}^c_{\rm rel} - V^c_{\mathcal{C}})\widetilde{\mathcal{G}}_c - 2\frac{df^c_{\rm reg}}{dr_c}\frac{\partial G_{l_c}}{\partial \rho_c}\frac{\Psi^c_{1\otimes 2}}{r_c} - \frac{d^2 f^c_{\rm reg}}{dr_c^2}\mathcal{G}_c \right\} d^{3A}R. \tag{4.23}$$

This is a reformulation of the same equations in Ref. [20]. Integration in these expressions takes place in the coordinates of all nucleons, $\mathbf{R}_i$ with $i = 1, ..., A$, in the center of mass frame. Once these coordinates are given, the value of $\mathbf{r}_c$ depends on the partition of nucleons into ψ_{c1} and ψ_{c2}, so that the cluster antisymmetrizer $\mathcal{A}_c$ in $\Psi^\dagger$ everything to the right of Ψ in the integrands. The integral relations to calculate the surface amplitudes A_c and B_c are then readily applied using VMC computed wave functions Ψ, ψ_{1c}, and ψ_{2c}. I evaluate integrals over the entire interior of the box at $r_c < 9$ fm using Monte Carlo importance sampling with weight function $\Psi^\dagger\Psi$; the short range of $\hat{V}^c_{\rm rel} - V^c_{\mathcal{C}}$ ensures that the integrand is zero in the outer parts of the box.

It is implicit in the derivation of the integral relations that Ψ, $\psi_{1c},$, and ψ_{2c} are exact eigenfunctions of their respective Hamiltonians. Our Ψ_V and ψ_{1c}, on the other hand, are variational approximations to these eigenfunctions. Previous experience in using integral relations with VMC wave functions [37, 38] supports their use despite this apparent shortcoming, because it produces results that compare well with experiment. Much of the utility of the method, in fact, arises from the circumstance that the interior part of Ψ_V, where the VMC ansatz is the most successful, is the only part that contributes to the integrals. I tried to estimate the size of the error due to deviations from $(H_1 - E_1)\psi_{1c} = 0$, but I found that the Monte Carlo sampling variances on those deviation terms swamped their actual size. Further progress on that question will presumably require modification of the sampling; past experience has essentially always been that proposed modifications are even worse than the standard sampling (e.g. Ref. [55]), so I chose not to pursue the question further at this time.

As mentioned in Chapter 1, Eqs. (4.23) and (4.22) can be viewed as $r \to \infty$ properties of the overlap of the wave function on channel c. A generalized version of Eq. (2.9) applicable at all radii is

$$R_c(r) = \frac{1}{r\mathcal{N}_V}\left\{\bar{A}_c(r)F_{l_c}(\eta_c, k_c r) + \bar{B}_c(r)G_{l_c}(\eta_c, k_c r)\right\}, \tag{4.24}$$

with

$$\bar{A}_c(r) \equiv \frac{2\mu}{\hbar^2}\int_{r_c<r} \Psi^\dagger(\hat{V}^c_{\rm rel} - V^c_{\mathcal{C}})\mathcal{G}_c \, d^{3A}R \tag{4.25}$$

$$\bar{B}_c(r) \equiv -\frac{2\mu}{\hbar^2}\int_{r_c<r} \Psi^\dagger(\hat{V}^c_{\rm rel} - V^c_{\mathcal{C}})\mathcal{F}_c \, d^{3A}R, \tag{4.26}$$

so that $\bar{A}_c(r \to \infty) = A_c$ and $\bar{B}_c(r \to \infty) = B_c$ (cf. Eq. (34) of Ref. [38]). Since Eq. (4.25) contains the same singularity that motivates the regularizer, the same problem has to be avoided here. I do that by computing the integral over all space using the regularizer (Eq. (4.23)) and then subtracting the portion of the unregularized integral located at larger radius,

$$\bar{A}_c(r) = A_c - \frac{2\mu}{\hbar^2}\int_{r_c>r} \Psi^\dagger(\hat{V}^c_{\rm rel} - V^c_{\mathcal{C}})\mathcal{G}_c \, d^{3A}R. \tag{4.27}$$

Eqs. (4.25) and (4.26) or their equivalents have been used in the literature to calculate cluster overlaps for Hartree-Fock and VMC wave functions [33, 38, 69]. In Ref. [38] it was found that for VMC wave functions Eq. (4.24) produces overlap functions that agree well with Eq. (4.2) at $r_c \leqslant 5$ fm, but that diverge from the direct calculation at large radius by going over to the correct asymptotic shapes for the specified E_c. This result can be interpreted as providing an extension of the accurate short-range part of the VMC ansatz into parts of the wave function that are more difficult to compute accurately with VMC, or at least within a given channel. Recall that the integrals in Eqs. (4.14), (4.15), (4.25), and (4.26) are short-ranged because the nucleon-nucleon pair and triplet interactions inside $V^c_{\rm rel}$ are short-ranged, and (for the cases of charged particles) $V^c_{\mathcal{C}}$ removes the monopole Coulomb interaction at large radius. For the present calculations, agreement between Eqs. (4.2) and (4.24) at small r is an important tool for code validation and interpretation of results.

To compute Eqs. (4.26), (4.23),and (4.24) using GFMC wave functions, I can use nearly the same infrastructure in the VMC/GFMC code that was used for overlaps. However, complications arise because the integral method requires the evaluation of $\hat{V}_{\rm rel}$. For the exact expressions in Eqs. (4.15) and (4.21), this does not pose an obvious problem. In GFMC, integral relations are a special case of off-diagonal calculations, where both right- and left-mixed estimates are required. In the VMC code where this operation is actually carried out, the A-body wave function is always on the right and the potential was previously only set up to operate toward the right. This leaves us unable to carry out mixed estimates of the form shown in Eq. (4.5) where we only have discrete samples on the right and thus cannot evaluate derivative operators. To solve this problem, I built the routines necessary to evaluate the application of the potential operators on the $\mathcal{F}_c$, $\mathcal{G}_c$, and $\tilde{\mathcal{G}}_c$, which are always constructed as "bra" objects on the left sides of Dirac brackets — I had to modify the potential routines so that they can act "toward the left" rather than "toward the right" in matrix element brackets. We can then compute the propagated estimates for Eq. (4.26) for the left,

$$\bar{B}_{c,L}(r;\tau) \equiv -\frac{2\mu}{\hbar^2}\int_{r_c<r} \Psi_V^\dagger(\hat{V}^c_{\rm rel} - V^c_{\mathcal{C}})\mathcal{F}_c(\tau)\, d^{3A}R, \tag{4.28}$$

and the right,

$$\bar{B}_{c,R}(r;\tau) \equiv -\frac{2\mu}{\hbar^2}\int_{r_c<r} [\Psi(\tau)]^\dagger(\hat{V}^c_{\rm rel} - V^c_{\mathcal{C}})\mathcal{F}_c(\tau=0)\, d^{3A}R. \tag{4.29}$$

analogously to the lower two lines of Eq. (4.5). Here, I have introduced the propagated regular channel-cluster function

$$\mathcal{F}_c(\tau) = \Psi^c_{1\otimes 2}(\tau)\frac{F_{l_c}(\eta_c, k_c r_c)}{k_c r_c} \tag{4.30}$$

in which the target nucleus has been GFMC propagated. To calculate the GFMC mixed estimate we apply Eq. 3.23,

$$\bar{B}_c(r;\tau) \approx \frac{\bar{B}_{c,L}(r;\tau)}{\mathcal{N}_L} + \frac{\bar{B}_{c,R}(r;\tau)}{\mathcal{N}_R} - \frac{\bar{B}_{c,V}(r)}{\mathcal{N}_V}. \tag{4.31}$$

The VMC quantities in Eq. (4.31) are denoted with a subscript V and they are analogous to expressions given earlier in Eqs. (4.2) and (4.3). Likewise we can calculate the propagated form of Eq. (4.27), $\bar{A}_c(r;\tau)$, which is found from the expression in Eq. (4.31) that gives $\bar{B}_c(r;\tau)$, *mutatis mutandem*. Additionally, we compute the GFMC surface amplitudes $A_c(\tau)$ and $B_c(\tau)$ by evaluating $\bar{A}_c(r;\tau)$ and $\bar{B}_c(r;\tau)$ at the surface.

We can then assemble $\bar{B}_c(r;\tau)$ and $\bar{A}_c(r;\tau)$ to evaluate the GFMC estimate for the integral method spectroscopic overlaps,

$$R_c(r;\tau) \approx \frac{1}{r}\left\{\bar{A}_c(r;\tau)F_{l_c}(\eta_c, k_c r) + \bar{B}_c(r;\tau)G_{l_c}(\eta_c, k_c r)\right\}. \tag{4.32}$$

As before in the VMC case the calculations of Eq. (4.5) and Eq. (4.32) are equivalent for accurately-computed wave functions, and in turn are a useful diagnostic tool. I have also implemented a test to evaluate pure-VMC integral relations when the potential acts on the cluster-product function instead of on the A-body function, even though this is unnecessary in the pure VMC calculation. The differences between the two methods are within Monte Carlo variance, so no significant problems are visible.

The procedure for computing QMC scattering observables via the integral method begins by computing VMC wave functions that minimize Eq. (3.8) separately for a scattering state and for the individual colliding nuclei. The optimized wave functions are then propagated to their near exact ground states using GFMC routines. This establishes both the VMC and GFMC channel energies E_c corresponding to the imposed boundary conditions. That E_c is used with the corresponding wave functions to evaluate the left, right and VMC estimates of the surface amplitudes (A_c and B_c). Scattering observables are computed from the resulting amplitudes. To obtain results at multiple energies, one repeats this procedure for many different boundary conditions that yield different E_c.

Chapter 5

Integral Method Verification and Regularizer Choice

In this section I verify the integral method by comparison of overlap functions between integral and direct calculations in the $n + {}^3\mathrm{H}$ system. I also introduce the fixed interior wave approximation and describe its advantages. Lastly, I outline how I choose my specific regularizer.

5.1 Verification

Comparing VMC overlap functions computed using Eq.(4.2) against those computed from Eq.(4.24) tests my implementation of the integral relations and identifies useful values of the regularization parameter γ. I carry out this test by examining the states in the $n + {}^3\mathrm{H}$ system computed from the AV18 potential alone, with the boundary conditions ζ_c chosen to give optimized variational energies E_V (c.m.) in the neighborhood of 3.0 MeV. At this energy, there is a broad resonant feature in the p-wave cross section.

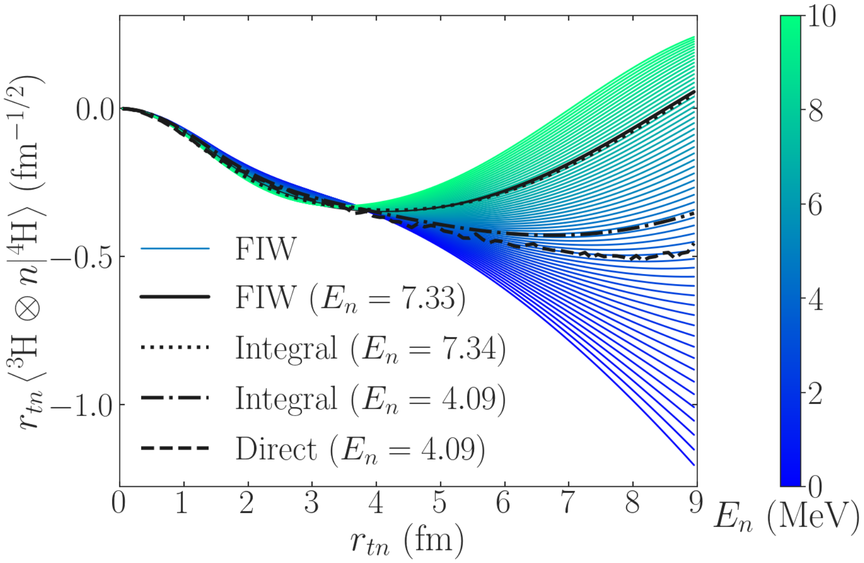

Figure 5.1: Overlap functions computed from a representative ${}^3P_0$ wave function with the AV18 interaction. These have been computed using the direct method of Eq. (4.2) (short-dashed, with "shot noise"), the integral method of Eq. (4.24) (dash-dotted), and the fixed interior wave (FIW) approximation (solid, energies distinguished by color). All curves except the dotted are computed from the same wave function with VMC energy corresponding to $E_n = 4.09$ MeV; the dotted curve shows the integral-method overlap (analogous to the dot-dashed curve) for a separate wave function with VMC energy corresponding to $E_n = 7.34$ MeV (rescaled to account for differences in normalization that arise from how the wave function fills the box). It is nearly identical to the FIW result at 7.33 MeV using the 4.09 MeV wave function, shown as a solid black line for visibility.

The direct overlap calculation of Eq. (4.2)) is carried out in the VMC code as a single Monte Carlo integration over all particle coordinates, in which the radial overlap integral at each r_{tn} is calculated from the accumulated samples in a finite-thickness (0.1 fm) bin [41]; this accumulation in shells is an implementation of the delta function in Eq. (4.2). In the figures, each neutron-triton separation, r_{tn} is identified as the midpoint of its shell. The integral-relation overlap of Eq. (4.24) is evaluated in a similar procedure carried out at the same time. The value of A_c is obtained from the regularized integral over all space in Eq. (4.23), and contributions to the integrals in Eqs. (4.27) and (4.26) at any r_{tn} consist of all Monte Carlo samples at smaller and larger radius, respectively. The optimized energy E_V is initially used to specify k_c and η_c in these integral calculations.

In Fig. 5.1 I focus on results of these calculations for a representative state in the ${}^3P_0$ scattering channel. After choosing the ζ boundary condition for this calculation, the center-of-mass energy E_{tn} was computed by VMC to be 3.07 MeV ($E_n = 4.09$ MeV). The dashed curve shows the direct overlap (Eq. (4.2)), while the dash-dotted curve shows the integral-method overlap (Eq. (4.24)). Each of these curves is shown multiplied by r_{tn} to remove a trivial source of radial dependence and give functions similar to solutions of a radial Schrödinger equation (e.g., Eq. (2.5)). Since the direct overlap at each radius is computed only from Monte Carlo samples that fall into a thin radial bin, the dashed curve displays "shot noise" that is visible as small fluctuations with radius. On the other hand, the integral method curve is smooth because at each r_{tn} it contains contributions from samples at all r_{tn}; There are many more samples involved and also many shared samples contributing to any two neighboring points on the curve.

5.2 Fixed Interior Wave Approximation

The dependence on E_c in $\mathcal{F}_c$ and $\mathcal{G}_c$ leads to an approximation procedure that avoids repeated energy minimizations. This approach builds on previous experience imposing experimental separation energies (or resonance energies) on the integral relations in Refs. [37, 38] even when they differed from computed energies. If there are no sharp resonances, the small-r_c part of a scattering wave function changes very little over an energy range of several MeV above threshold; this is a consequence of E_c being small relative to the potential strength and (at least in some cases) of antisymmetry constraints on the wave function. Then I expect that nearly all the evolution of the A_c and B_c amplitudes with energy comes from the dependence of F_l and G_l on the channel energy E_c inside Eqs. (4.22) and (4.23).

The colored curves in Fig. 5.1 demonstrate application of the fixed interior wave (FIW) approximation to overlap functions. For each of those curves, I take the single optimized

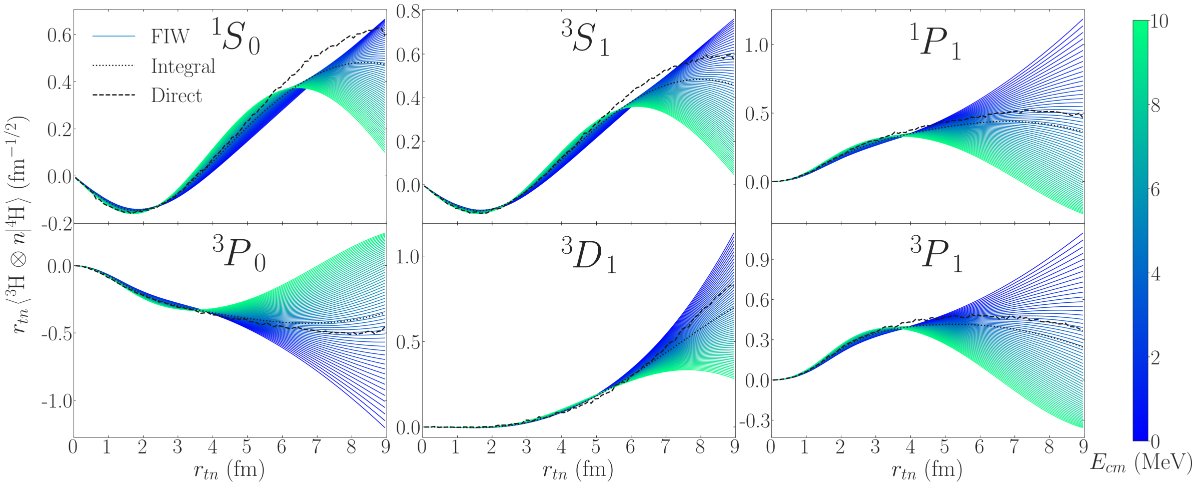

Figure 5.2: Overlap functions computed with AV18 for various partial waves of neutron-triton scattering using the same methods and symbols as Fig. 5.1. Qualitative matching in the interior range is present for each channel between direct and integral overlaps (dotted).

VMC wave function that produced the short-dashed and dot-dashed curves, but I use a different input energy for the integral relations. From the single variational wave function, this method generates approximate overlap functions over the entire low-energy spectrum from threshold to $E_n = 10$ MeV. (No attempt has been made to rescale the wave function to unit norm inside the box for the revised probability densities implied by the new R_c.) Each of these curves is consistent with the directly computed overlap at $r < 5$ fm. (See Sec. 5.3 for the dependence of this statement on the choice of γ.) The dotted curve shows the overlap using the integral method (not FIW) for the higher energy variational wave function that gave $E_n = 7.34$ MeV; it is nearly identical to the solid black curve, which was generated from the 4.09 MeV wave function using 7.33 MeV in the FIW approximation. These results are not unique to the $^3P_0$ channel; Fig. 5.2 shows similar results for other partial waves.

The many curves (often visible as shaded regions rather than individual curves) in Fig. 5.1 illustrate a further point concerning the use of fixed interior waves: It is a very efficient use of both computer and human resources. Computed directly from the definition, each of the 60 solid (shaded) lines in Fig. 5.1 would require a separate wave function with a different boundary condition and separate optimization. Instead, they have been computed from the integral relations for R_c from a single wave function. By skipping the separate wave function optimization followed by Monte Carlo walk generation (which involves recomputing wave functions) at every energy, the amount of work has been greatly reduced, especially for coupled channels.

In my subsequent neutron-alpha phase shift calculations described in Chapter 6.2, I improved the FIW approximation compared with my neutron-triton calculations. In neutron-triton, I regarded FIW as something to be applied to one wave function at a time, effectively extrapolating outward from a single phase shift point. In the neutron-alpha calculations, I have developed it into an interpolation method to be used in the energy region between two directly-computed wave functions. The fixed interior wave interpolation (FIWI) is as follows: given two QMC (two VMC or two GFMC) wave functions at the ends of an energy interval, FIW amplitudes are computed from each wave function using the energy at the midpoint of the interval. I then average the resulting K-matrix ($\tan\delta$) from each calculation so that $K_{\rm mid}{=}(K_1(E_{\rm mid}){+}K_2(E_{\rm mid}))/2$, the midpoint is found to lie on the expected trend. The main justification for this method is that it works slightly better in the neutron-alpha case than the original FIW approximation.

5.3 Regularizer Choice

Agreement between the overlap-computation methods at $r < 5$ fm is important because this is the region where the VMC wave function is most reliable. In that region, iterated pair correlations and antisymmetrization provide a structure that is not dominated by one or two elements of the variational ansatz, and it is where most of the power of the VMC method arises. The $r < 5$ fm region also typically contains the largest number of Monte Carlo samples. We therefore expect the directly computed overlap to be rather accurate there. In this region the integral method should be unable to improve significantly on the directly computed overlap, and we expect the two methods to agree there if the integral method has been successfully implemented. In Figs. 5.1 and 5.2 the integral (dash-dotted black curve) and direct (short-dashed) overlaps are, in fact, nearly identical between 0 fm and 5 fm.

This match between the methods provides a vital test of the regularizer for G_l, which in turn affects both the accuracy and variation of scattering calculations [24]. In carrying out the present work, I tried several possible regularizing functions, but I found Eq. (4.19) to be by far the most successful in reproducing overlap functions. All the results that I show are computed with that regularizer, and it is also the one used in recent calculations with the hyperspherical harmonics method [24] and in solving the 5-body Faddeev-Yakubovsky equations [9]. The results shown are all computed with a specific value of the regularization parameter γ, and now I describe how it was chosen.

If γ is chosen too small, the regularizer has effects at the box surface that violate assumptions behind Eqs. (4.23) and (4.27) (essentially, Eq.(4.20)). If it is chosen too large, the regularizer does not adequately remove the harmful effects of the singularity in Eq. (4.14). In Fig. 5.3 I vary γ over the range 0.01 to 2.0 fm^{-1} for overlap calculations of a single state $^3P_0$, and I also show the overlap from the direct method. Color indicates the value of γ, with the color scale chosen to emphasize values where the methods agree. I quantify the agreement between the two methods with a sum of square errors (SSE) statistic in the $r < 5$ fm region. The SSE is given by

$$\mathrm{SSE}_c(\gamma) \equiv \sum_{i=1}^{n_r} \left[r_i R_c^D(r_i) - r_i R_c^I(\gamma, r_i) \right]^2 , \tag{5.1}$$

where R^D is the directly computed overlap of Eq. 4.2, R^I is the integral-method overlap of Eq. 4.24, and the sum extends over the 0.1-fm-thick bins that define neutron-triton separations in the direct calculation. I continue to work with rR_c rather than R_c, because it reduces the weight in Eq. (5.1) of poorly-sampled low-volume shells near $r = 0$ and reduces the severity of divergence of G_l near the origin in the Eq. (4.27) integrand.

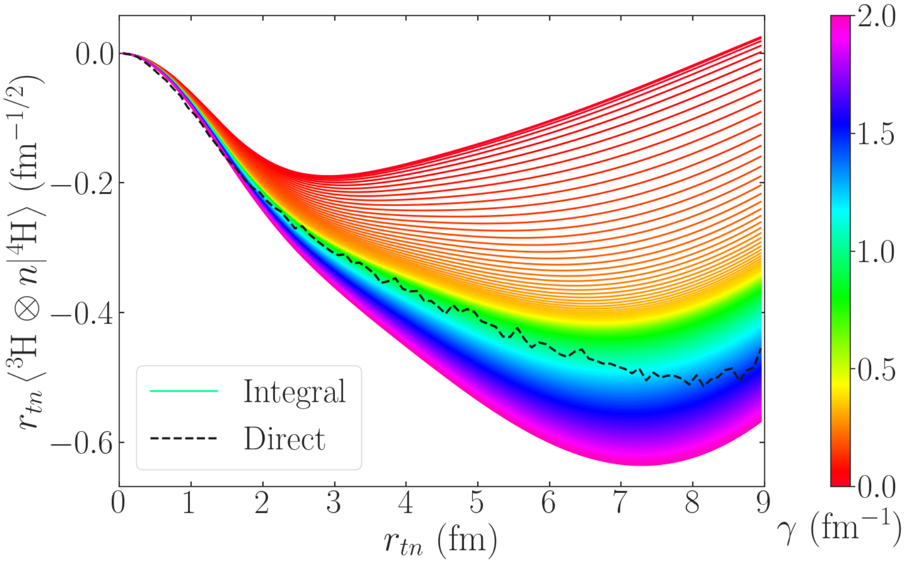

Figure 5.3: The effect of the regularization parameter γ on the overlap function $r_{tn}R_c(r_{tn})$ for a ${}^3P_0$ state in neutron-triton scattering at $E_n = 4.09$ MeV with AV18. The dashed curve shows the result of calculation from the definition, while the solid curves are the results of integral-method calculations with varying γ. Values of γ run from 0.01 to 2.0 fm^{-1} and are indicated by color. Values between roughly 0.4 and 1.4 fm^{-1} produce close agreement between methods in the region where VMC is most accurate, and I choose 0.625 fm^{-1} for further AV18 calculations.

In principle, I could choose a different gamma for each channel, but the SSE evaluation in Fig. 5.4 reveals a single range that works well for many channels in neutron-triton scattering, and I see little value in further fine-tuning for individual channels. For AV18 I find that $\gamma = 0.625\ \mathrm{fm}^{-1}$ minimizes the SSE for all neutron-triton and neutron-alpha cases examined and lies in a "stationary" range of weak γ dependence. Repeating the analysis for the Norfolk NV2+3-Ia interaction in $n + {}^3\mathrm{H}$ gives a slightly smaller best γ, with the stationary range centered on 0.52 fm^{-1}. At 4 MeV, I find that varying γ through the stationary SSE range in VMC only changes phase shifts by $\leqslant 2$ degrees relative to the optimal γ for both of these potentials and systems.

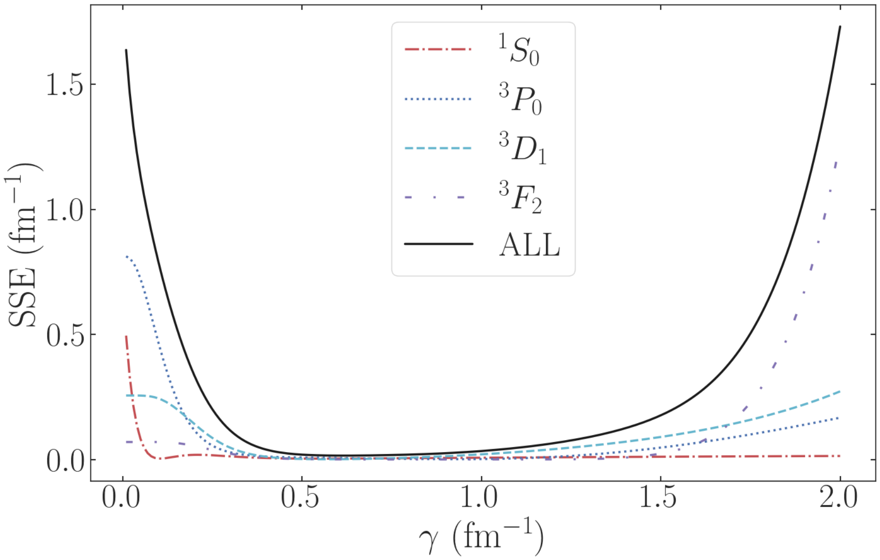

Figure 5.4: Comparison between direct and integral-method overlap calculations for four states in different neutron-triton channels near $E_n = 4$ MeV at varying γ. Agreement is quantified by the sum of square errors at $r < 5$ fm defined in Eq. (5.1), SSE(γ), applied separately to each channel and to a sum over all four channels. Small SSE indicates agreement between methods when γ is small enough to regularize G_l effectively at the origin but large enough not to affect the box surface. This occurs in the flat region between 0.5 and 1.0 fm^{-1}.

Chapter 6

Results

I now present the results of scattering calculations using the direct method and the integral method to determine overlaps, phase shifts, and cross sections. For neutron-triton scattering, these results are computed entirely from VMC, and some pairs of coupled angular momentum channels are treated. Neutron-alpha scattering was examined with both VMC and GFMC calculations. Since it is customary in the recent literature on $A = 4$ systems to quote laboratory energy rather than center-of-mass energy, I present most $n + {}^3\mathrm{H}$ results in terms of the neutron energy when the target is stationary,

$$E_n = \frac{4}{3} E_{\text{c.m.}}. \tag{6.1}$$

This expression neglects the small correction arising from the binding energy and from the difference of the proton from the neutron mass.

6.1 $n + {}^3$H

6.1.1 Single-channel cases

I begin by showing the single-channel, $J^\pi = 0^+$ and 0^-, phase shifts for neutron-triton scattering computed from the AV18 potential in Fig. 6.1 and from the newer Norfolk-Ia interactions in Fig. 6.2. For comparison with my calculations, I show results for AV18 using the hyperspherical harmonics method [3] as black squares. These are well-benchmarked against other methods and can be regarded as essentially exact; any accurate calculation from AV18 should match them closely. I also show as a solid curve empirically-derived phase shifts that were computed by fitting the much more extensive $p + {}^3$He data to a phenomenological R-matrix model and applying isospin symmetry [70]. (The isospin-rotation procedure mainly involves replacing Coulomb functions with spherical Bessel functions and shifting the level energies by a phenomenological difference of Coulomb interaction energies between the two systems.)

The direct method of computing phase shifts from VMC (circles in Fig. 6.1) reproduces qualitative features of the phase shifts for both of these partial waves. However, the phase shift at fixed energy comes out too low by typically 10° for s-wave and 5° for p-wave states. The variational principle implies that the computed energy is higher than the true energy for any boundary condition ζ, so Eq. (4.1) in general gives curves that can be viewed as being either too low in phase shift or too high in energy [30]. Failure to match the exact result reflects limitations of the variational ansatz (or else failure to optimize it well). Until this work, the main option to improve on the direct calculation from a VMC wave function has been to use the VMC wave function as the starting point for a GFMC calculation [25, 31]; GFMC then finds the correct energy for the given boundary condition more accurately before computation of the phase shift.

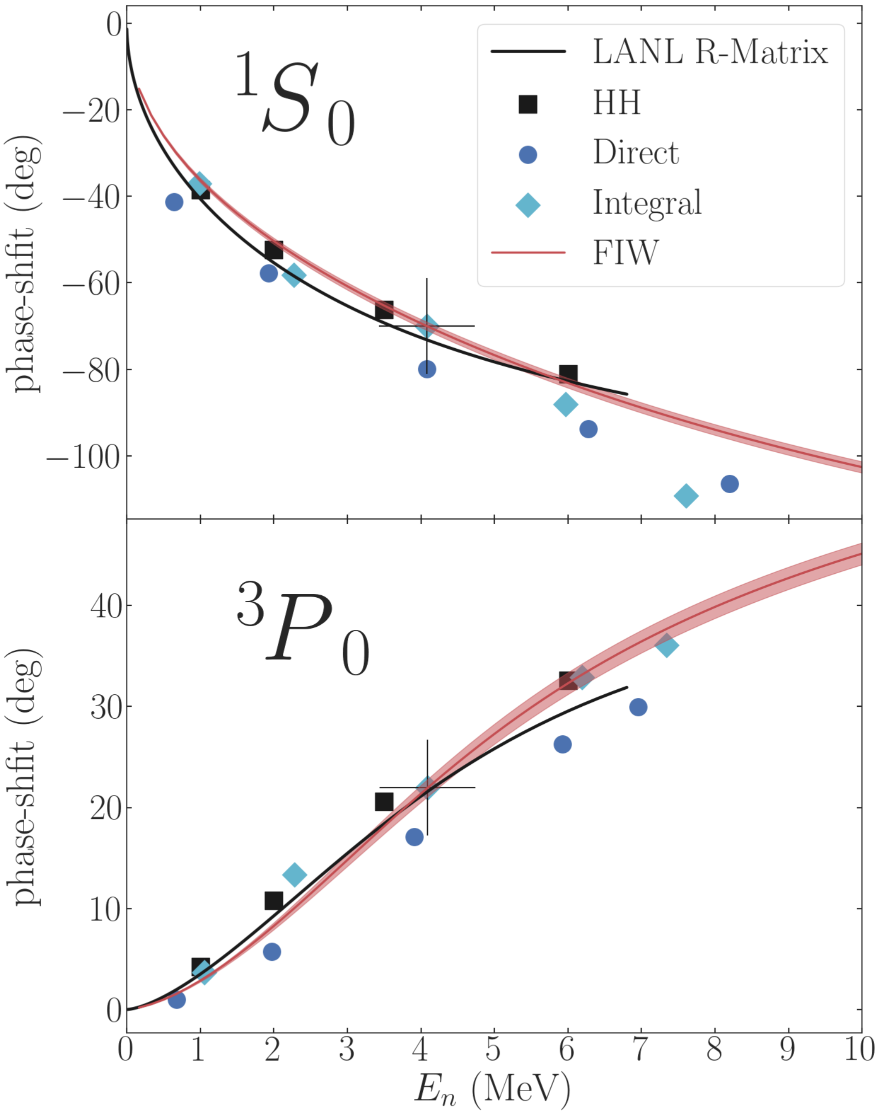

Figure 6.1: Single-channel phase shifts (in degrees) for $n + {}^3\text{H}$ with the AV18 potential, computed from VMC using the direct method (blue circles), the integral method (cyan diamonds), and fixed interior waves (red band). The width of the band indicates the Monte Carlo sampling error. For comparison I show an empirical R-matrix model (solid black curve labeled "LANL R-Matrix," explained in the text) [70] and essentially exact results from the hyperspherical harmonic method [3] with the same potential (black squares). The plus symbol indicates the VMC wave function chosen to provide the fixed interior wave for computations of the red band.

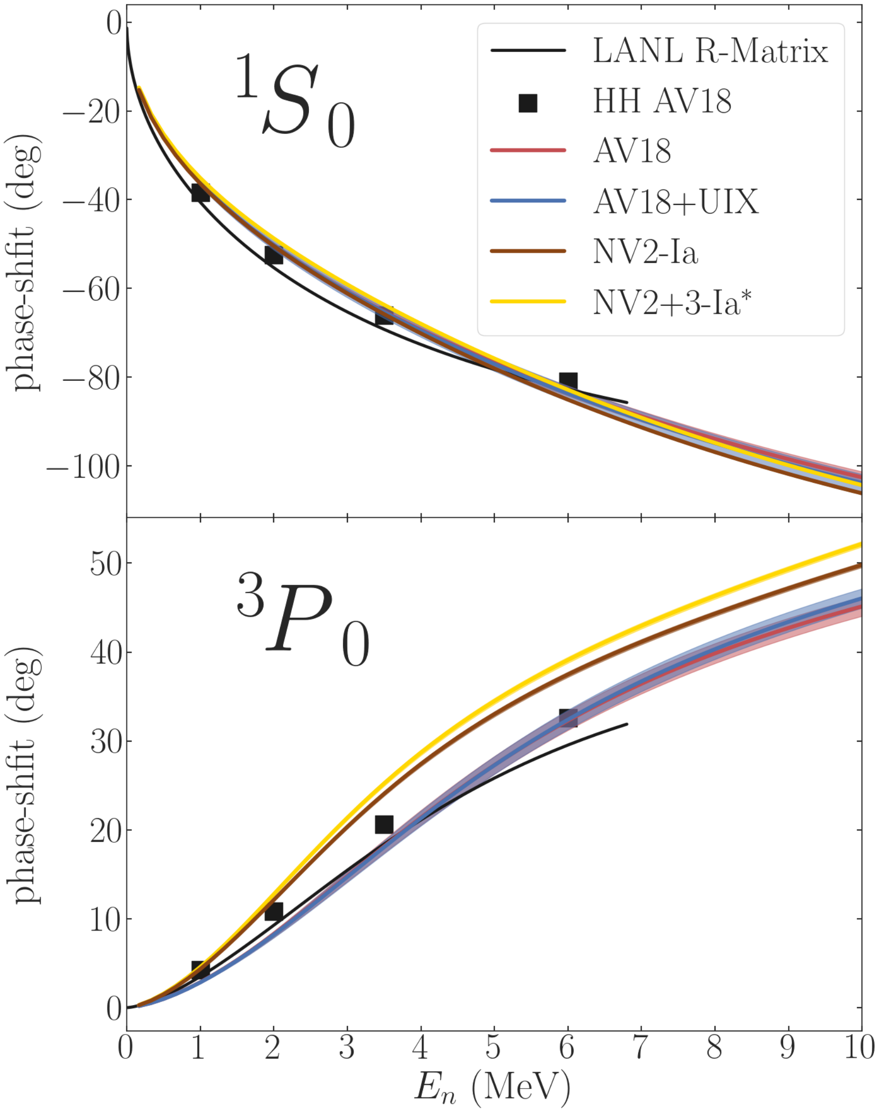

Figure 6.2: Single-channel phase shifts (in degrees) for $n + {}^3$H in the FIW approximation for multiple interactions, with and without three-nucleon terms. The R-matrix curve and AV18 benchmark calculation are as in Figs. 6.1. The Norfolk Ia interaction both with and without the Ia* three-body terms shows somewhat larger attraction in the p-waves than both the AV18-based calculations (with and without Urbana IX three-body terms) and the empirically-derived phase shifts. Widths of the bands show Monte Carlo sampling errors.

The diamond shapes in Fig. 6.1 show results of applying the integral relations in Eqs. (4.22) and (4.23) to VMC wave functions and using the single-channel relation $\tan\delta_c = B_c/A_c$. The energy assumed in the integral relations is equal to the variational energy of each state. These results are in much closer alignment with the exact results, but with some scatter away from their trend for individual VMC points. The scatter presumably reflects the quality of each wave function optimization. The energy used in computing both the circles and the diamonds is measured relative to a neutron and triton at rest infinitely far apart. For this I take the difference of computed VMC energies between the scattering state and my best VMC triton wave function (rather than, e.g., the exact triton energy for AV18).

Finally, in each partial wave I apply the FIW approximation by choosing one VMC solution (marked in the graphs with a cross) and computing integral-relation phase shifts at all energies from that single wave function. The result is shown as the red curve with shaded band corresponding to Monte Carlo statistical errors on the integrals. By its construction the red curve passes through the point with the cross on it, which was chosen for its location in the middle of the energy range of interest. Table 6.1 shows that the results are within 2.5° of exact phase shifts for AV18. Inspection of ${}^3P_0$ phase shifts in Fig. 6.1 suggests that better results might have been obtained by choosing the wave function for FIW treatment based on how well it matches exact results; even without exact results for comparison, a wave function with outlying low phase shifts relative to the trend of other VMC points could be avoided as possibly poorly-optimized. Nonetheless, deviation of the p-wave phase shifts from the trend of both the R-matrix model and the benchmark indicates that the FIW loses accuracy when it proceeds too far above the energy of the wave function used; this appears to happen around 6 MeV in the present case.

These results establish the integral method and its variant with fixed interior waves as useful ways to obtain approximate phase shifts from VMC wave functions. The combination of integral relations with VMC wave functions evidently does not quite achieve the precision available with other computational frameworks in the $n + {}^3$H system. However, it greatly improves both the quality and the efficiency of possible scattering calculations using VMC, which might be more readily applied to larger systems than the other solution methods.

6.1.2 Coupled channels

Proceeding to other neutron-triton partial waves in Fig. 6.3, I show only results with fixed interior waves, always generated from one VMC wave function per channel near 4 MeV. The remaining partial waves relevant at low energy come in three pairs of coupled channels, though the channel coupling is extremely weak in the 1^+ and 2^- states (where it arises from the tensor force); the coupling is somewhat stronger between the two spin combinations in the p-wave states with $J^\pi = 1^-$. Phase shifts and the largest mixing parameter from Fig. 6.3 are given in Table 6.1 at the energies of published benchmark calculations [3].

Considering only AV18 for the moment, I find good agreement with the benchmark for all of the phase shifts except in the ${}^1P_1$ channel, where the curve is qualitatively different from both the benchmark and the empirically-derived curve. I obtain very similar results when I carry out the calculation with other potentials, suggesting some systematic problem with my calculations in this specific channel. After extensive checking, I have been unable to find a coding error, and I suggest tentatively that it may be a shortcoming of the variational ansatz specific to this configuration; specifically it could be related to the failure of linear independence between the wave function pair involved. It will be informative in the near future to see if the problem persists in GFMC calculations that use the VMC solutions here as starting points.

The 1^+ mixing parameter is very small in both my AV18 calculation and the hyperspherical harmonics calculation, smaller than 2.5°. In that sense there is good agreement, though the VMC results are about half the size of the hyperspherical result. For 1^- states the VMC

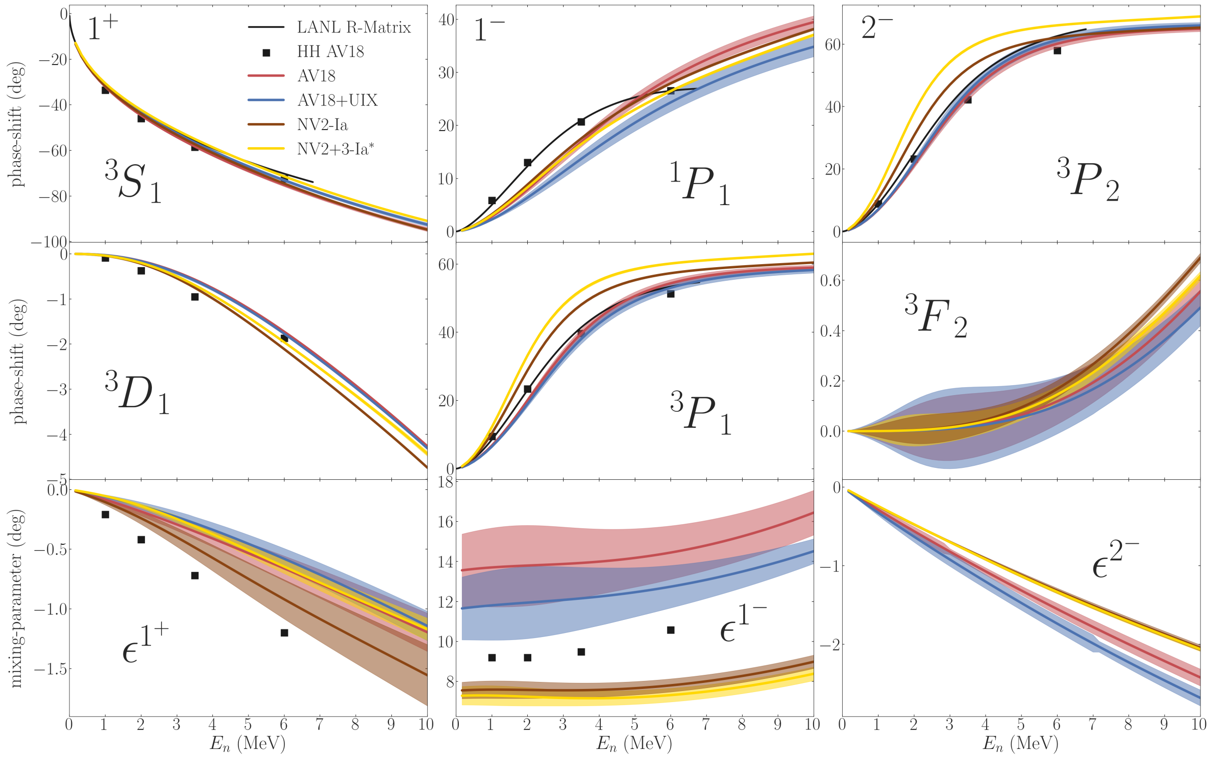

Figure 6.3: Phase shifts and mixing parameters (in degrees) for $n + {}^3\text{H}$ in the FIW approximation with the same interactions as Fig. 6.2. The R-matrix curve and AV18 benchmark calculation are as in Figs. 6.1 and 6.2. The AV18 phase shifts are within 2.5° of the benchmark, except for an apparent difficulty shared by calculations with all potentials in the $^1P_1$ channel. Widths of the bands show Monte Carlo sampling errors.

Table 6.1: $n + {}^3\mathrm{H}$ phase shifts and mixing parameters for S- and P- waves computed using the FIW approximation for various interaction models. The hyperspherical harmonics (HH) results are from Ref. [3].

	$^1S_0$	$^3P_0$	$^3S_1$	$^3P_2$	$^1P_1$	$^3P_1$	ϵ^{1-}
1.0 MeV							
HH AV18	−38.44	4.26	−33.57	8.82	5.87	9.44	9.19
AV18	−36.3(5)	2.9(1)	−32.1(3)	7.0(3)	2.8(2)	6.8(3)	13.7(19)
AV18+UIX	−36.2(8)	2.8(1)	−31.1(2)	7.1(4)	2.3(2)	6.5(3)	11.8(17)
NV2-Ia	−36.40(9)	4.34(5)	−31.71(6)	10.6(1)	3.24(4)	10.4(1)	7.6(4)
NV2+3-Ia*	−35.12(9)	4.57(6)	−0.04(1)	12.2(2)	3.08(5)	13.7(2)	7.3(5)
2.0 MeV							
HH AV18	−52.41	10.82	−46.04	23.21	13.00	23.39	9.19
AV18	−50.3(7)	8.3(3)	−44.7(4)	21.3(10)	7.95(51)	20.0(8)	13.8(20)
AV18+UIX	−50.3(11)	8.2(3)	−43.3(3)	21.9(12)	6.4(7)	19.0(8)	11.9(18)
NV2-Ia	−50.5(1)	12.1(1)	−43.92(8)	30.8(3)	8.86(11)	28.9(3)	7.6(4)
NV2+3-Ia*	−48.7(1)	12.8(2)	−0.20(1)	38.1(5)	8.35(12)	33.3(5)	7.2(5)
3.5 MeV							
HH AV18	−66.14	20.61	−58.53	42.22	20.68	39.63	9.48
AV18	−65.3(9)	18.1(7)	−58.3(5)	43.6(17)	16.9(9)	39.6(13)	13.9(17)
AV18+UIX	−65.4(14)	18.1(7)	−56.5(5)	44.8(19)	13.7(12)	38.0(14)	12.2(16)
NV2-Ia	−65.8(2)	24.1(3)	−57.3(1)	52.1(3)	17.5(2)	48.1(4)	7.6(4)
NV2+3-Ia*	−63.7(2)	25.2(3)	−55.0(1)	58.6(4)	16.5(2)	52.3(5)	7.2(4)
6.0 MeV							
HH AV18	−81.05	32.61	−72.40	57.94	26.55	51.27	10.57
AV18	−83.2(11)	32.3(11)	−75.2(7)	60.1(13)	29.0(12)	54.4(11)	14.4(13)
AV18+UIX	−83.7(17)	32.4(11)	−73.1(6)	61.3(15)	24.3(17)	53.0(12)	12.7(11)
NV2-Ia	−85.1(2)	37.5(3)	−74.5(2)	62.1(2)	27.9(2)	57.3(3)	7.8(3)
NV2+3-Ia*	−82.9(3)	39.1(3)	−71.4(2)	66.0(3)	26.5(4)	60.2(3)	7.3(3)

mixing parameter comes out somewhat larger (roughly 14° instead of 10° over the whole energy range) but they are of similar magnitude, and one of channels here is the $^1P_1$ channel where something has apparently gone wrong in my VMC calculations as discussed above.

6.1.3 Three-nucleon and chiral potentials

In addition to the AV18 potential alone, I also carried out calculations that combine the AV18 two-body potential with the Urbana IX (UIX) three-nucleon interaction [26, 58], and that use the Norfolk family of local chiral potentials [71, 72]. Results for AV18+UIX and for the NV2-Ia and NV2+3-Ia* potentials are shown alongside the AV18-only results in Figs. 6.2 and 6.3 and in Table 6.1. These two Norfolk potentials differ in their inclusion or not of three-nucleon terms and in what data were used in fitting them; NV2-Ia consists only of two-body terms, while NV2+3-Ia* includes a three-body interaction. It is evident from the phase shift graphs that while results in other channels are very similar between potentials, the Norfolk interactions provide somewhat larger attraction in the p-wave channels than appears to be supported by the isospin-symmetry-based R-matrix curve. No strong qualitative dependence on three-body terms is evident in the cases shown, though there is some difference. Qualitative agreement of all calculations in the s-wave channels is not surprising, since s-wave scattering in this and many light systems has the character of scattering from a hard sphere, due to antisymmetry constraints on the wave function [25, 73].

I show total cross sections for these interactions and for two others in Fig. 6.4. In the left panel, I show results for AV18 alone and for AV18+UIX; I also show results for AV18 with the Urbana X three-nucleon interaction, which has a very similar structure to Urbana IX but has been tuned to produce binding energies closer to those of the more computationally expensive Illinois-7 interaction [74]. Although AV18+UIX produces very similar results to AV18 alone here, it is evident that a different choice of three-nucleon interaction could have

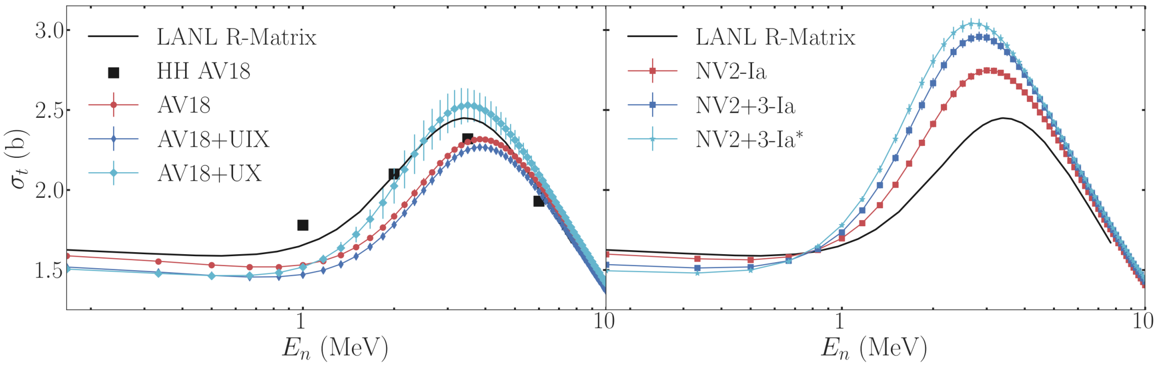

Figure 6.4: $n + {}^3\text{H}$ total cross section (in barns) as a function of neutron energy for various interactions. The left panel shows results for AV18 with and without the Urbana IX or Urbana X three-body terms. The right panel shows the Norfolk Ia potential with and without the Ia or Ia* three-body terms; error bars show Monte Carlo statistical uncertainties. Other symbols are as in Fig. 6.1 except that the LANL total cross section is from Ref. [75]. In general, the Norfolk Ia interactions give somewhat too-pronounced resonance structures in p-waves, while s-wave scattering correlates mainly with triton binding energy regardless of potential.

a noticeable effect on the p-wave peak around 3 MeV. The right panel shows total cross sections for NV2+3-Ia* and for NV2+3-Ia, which have three-body terms tuned to match differing input data. Here the choice of three-body interaction also has a significant effect on the resonance structure in the p-waves. In general, AV18 and AV18+UIX underpredict the strength and width of the resonance feature while all of the Norfolk interactions overpredict them.

6.1.4 Zero-Energy Limit

I summarize my s-wave calculations for a large collection of potentials by presenting total cross sections σ_t for thermal neutrons and coherent scattering lengths a_c in Table 6.2. These are computed from the singlet and triplet s-wave phase shifts via Eqs. (2.21) and (2.22), applying integral relations with $E_{\text{cm}} = 0.025$ eV to the usual fixed interior wave in each channel with variational energy $E_n \simeq 4$ MeV. I found no significant evolution of $\sigma_t(E)$ below

10 eV. As indicated in Table 6.2, the total cross section has been measured to below 50 keV and extrapolated to thermal energies yielding a result of $\sigma_t = 1.70 \pm 0.03$ b [46]. The two most recent measurements of the experimental coherent scattering length [76, 77] were carried out by the same group, with a more advanced setup for the second measurement. A third empirically-derived coherent scattering length comes from essentially the same Coulomb-corrected R-matrix calculation shown in my graphs [70].

Table 6.2: $n + {}^3$H Thermal-neutron cross section σ_t (in barns), coherent scattering length a_c (in fm), and ^{3}H binding energy (in MeV) computed in VMC with various interactions. The VMC phase shifts are computed in FIW approximation at $E_{\rm cm} = 0.025$ eV using wave functions of variational energy $E_n \approx 4$ MeV. For comparison I show values from the essentially exact hyperspherical harmonic (HH) method for AV18 and AV18+UIX, for the Coulomb-corrected R-matrix, and from experiment.

Interaction	σ_t	a_c	B_3
AV18	1.632(12)	3.598(27)	7.484(2)
AV18+UIX	1.558(13)	3.513(29)	8.277(2)
AV18+UX	1.543(15)	3.496(32)	8.254(6)
NV2-Ia	1.648(3)	3.615(6)	7.602(9)
NV2-Ib	1.656(3)	3.622(7)	7.339(9)
NV2-IIa	1.614(4)	3.579(9)	7.715(5)
NV2-IIb	1.734(68)	3.71(15)	7.646(14)
NV2+3-Ia	1.579(5)	3.535(10)	8.179(9)
NV2+3-Ib	1.558(4)	3.515(8)	8.170(15)
NV2+3-IIa	1.539(3)	3.494(6)	8.193(10)
NV2+3-IIb	1.566(8)	3.522(18)	8.236(14)
NV2+3-Ia*	1.536(3)	3.490(7)	8.205(8)
NV2+3-Ib*	1.580(5)	3.538(11)	8.161(14)
NV2+3-IIa*	1.544(5)	3.498(10)	8.218(17)
NV2+3-IIb*	1.557(5)	3.513(10)	8.212(22)
HH [24, 68]			
AV18	1.85	3.83	7.624
AV18+UIX	1.73	3.71	8.479
R-matrix [70]	-	3.607(17)	-
EXPT.	1.70(3) [46]	3.82(7) [76] 3.59(2) [77]	8.475 [78]

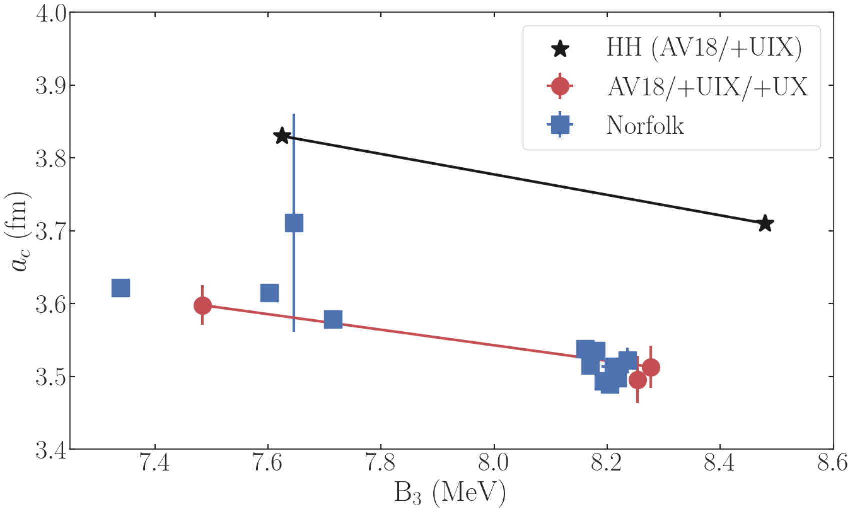

Figure 6.5: The $n + {}^3$H thermal neutron total cross section (in barns) coherent scattering length (in fm) as a function of VMC-computed triton binding energy (see text) ($\mathbf{B}_3$ in MeV) for various interactions. My VMC calculations of this line produce the same slope as the near-exact HH calculations (black squares) for two interactions.

Overall, the results in Table 6.2 depend only slightly on potential. It is known that the triton binding energy B_3 in a given model correlates with the s-wave phase shifts, analogously to the "Phillips line" that correlates B_3 with the neutron-deuteron scattering length when potentials are varied [79]. The VMC results in Table 6.2 support a reliable negative-slope correlation between B_3 and a_c, with B_3 taken not as the exact value for the potential but as my best-optimized variational result. The hyperspherical harmonics results for AV18 with and without Urbana IX suggest a correlation that has the same slope I find but is offset by about 0.2 fm in scattering length, presumably reflecting the same difference in precision between VMC/FIW and exact results seen above. Considering the offset from the hyperspherical harmonics calculations, it would appear that in general values for a given potential can be estimated by adding about 0.2 fm to a_c or 0.2 b to σ_t computed from VMC/FIW. Essentially, all the differences among the Norfolk potentials in Table 6.2 are attributable to the correlation between the VMC-optimized (not exact) B_3 and a_c.

6.2 $n + {}^4$He

I now turn to neutron-^{4}He scattering to test implementation of the integral method in GFMC calculations. This section presents calculations done only with the two-body AV18 interaction, which is well-benchmarked. I compare results against the 2007 calculations from Ref. [25] to judge success. Those older GFMC calculations differ from current direct GFMC results mainly by an iterative procedure in Ref. [25] that forced consistency between outer parts of $\Psi(0)$ the final GFMC energy. I have not followed that procedure because it consumes a large amount of effort for a small benefit that was expected to be unnecessary with the integral method. Moreover, the improved implementation of the boundary condition described below Eq. (3.10) made the variational wave function more consistent with the GFMC energy to begin with.

6.2.1 Energies

I begin with the GFMC energy expectation values as a function of imaginary time τ with $\Delta\tau = 0.0005$ MeV^{-1} to demonstrate the stabilization of the propagated energy. The first energy to establish is the alpha-particle energy, as I need it to establish threshold. In Fig. 6.6 I show the bound ^{4}He energy as a function of τ computed with the AV18 potential (perturbatively corrected AV8$'$). As expected, the propagated energies (black circles with error bars) quickly remove the high-energy contamination from the VMC energy (blue band) and approach a stable value at large τ, estimated by the average shown as a red band. Although the energy obtained from the VMC code and the $\tau = 0$ energy obtained from the GFMC code for the same wave function should be the same, there is a visible difference because of sampling variance between two Monte Carlo calculations. The energy from the VMC code is almost always lower because the wave function parameters are optimized on the same VMC samples that were used to estimate the energy. The VMC alpha binding

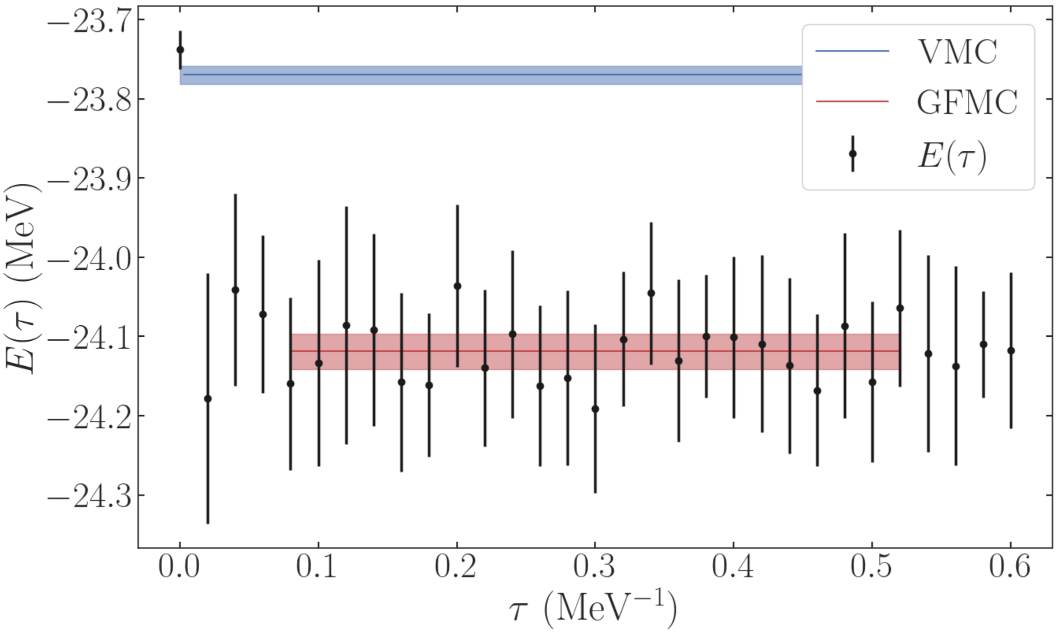

Figure 6.6: Ground state ^{4}He quantum Monte Carlo energy expectation values (in MeV) as a function of imaginary time (τ) for the AV18 nuclear interaction. The wave function yielding the variational Monte Carlo estimate (solid blue line with error band) and the $\tau = 0$ value for Green's function Monte Carlo constitute the initial starting point for GFMC. Energies are computed at intervals of $40\Delta\tau$, from walkers that have been allowed to propagate unconstrained for 25 steps before the evaluation. Each energy expectation value shown as a black dot is an average over Monte Carlo samples at the indicated τ. The horizontal red line and error band are the average of those expectation values from $\tau = 0.08$ to 0.52 MeV^{-1}. The GFMC method quickly removes high-energy contamination from the initial VMC wave function.

energy I computed with this potential is −23.77(1) MeV compared to the GFMC result of −24.12(2) MeV, which is in excellent agreement with previously benchmarked QMC results [57] and recent hyperspherical harmonic method calculations [68].

Moving on to unbound systems, low-energy scattering of neutrons from alpha particles is dominated by three completely uncoupled partial waves, with $J^\pi = 1/2^+$, $1/2^-$, and $3/2^-$. The positive parity channel is an s-wave (L=0), and the negative parity cases are p-waves (L=1). The process of computing energies is nearly identical in every channel, so I present only the procedure in the $1/2^+$ channel in Fig. 6.7. I begin by optimizing a VMC wave

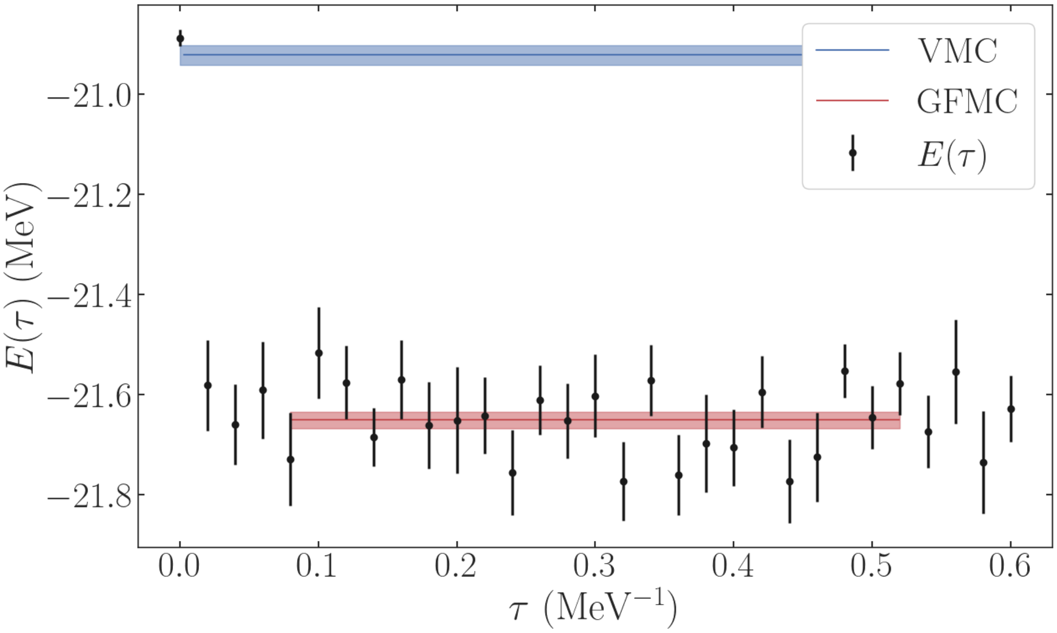

Figure 6.7: GFMC energy propagation of a scattering state in the ^{5}He 1/2+ system for AV18. The boundary condition is $\zeta = -0.13$ fm^{-1} at 9 fm, and symbols are as in Fig. 6.6. In this case energies were computed every 40 steps using walkers that had propagated 80 final steps without constraint.

function for a specific boundary condition ($\zeta = -0.13$ fm^{-1} at 9 fm) and then propagating that wave function according to Eq. 3.11. Similar to the bound case, the energy expectation value depends on τ, and I show this for the representative 1/2+ state in Fig. 6.7.

The propagated energy of the unbound state reaches stability similarly to the bound state. Similar plots are shown for several 1/2+ states in Fig. 6.8. In every case, GFMC evolution finds a stable energy, which can be used in the direct method to find a phase shift for the corresponding ζ.

6.2.2 Spectroscopic Overlaps

Next, I use the spectroscopic overlaps of GFMC wave functions to validate my calculations by the integral method. For the integral method calculations in neutron-alpha I found that

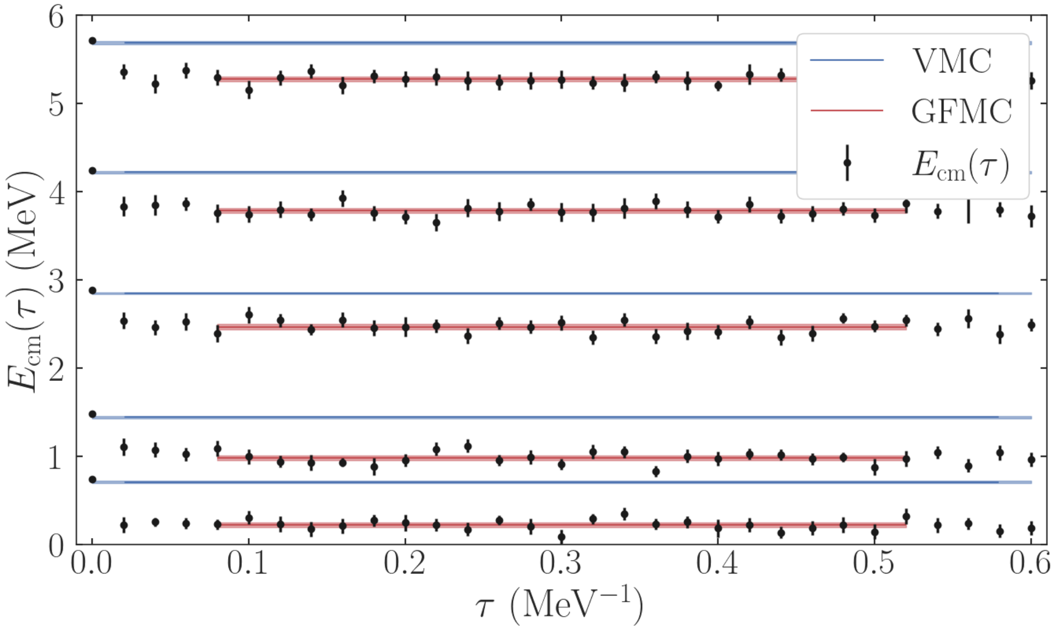

Figure 6.8: Energies relative to threshold of $n + {}^4\mathrm{He}$ scattering states with $J^\pi = 1/2^+$ (in MeV) as functions of imaginary time (τ) for the AV18 nuclear interaction and various boundary conditions. Each choice of ζ has its own set of energy values. Symbols and methods are as in Figs. 6.6 and 6.7. GFMC quickly settles on a stable energy corresponding to that boundary condition in each case.

the same regularizer ($\gamma = 0.625$ fm^{-1}) as neutron-triton minimized the SSE of all channels. I show the evaluation of direct overlaps from Eq. (4.5) and integral-relation overlaps from Eq. (4.32) in Figs. 6.9, 6.10, and 6.11 for $1/2^+$, $1/2^-$, and $3/2^-$ partial waves, respectively. The VMC overlaps are colored blue and the GFMC red. The integral method results are shown as solid curves with statistical error bands, and the circles show the direct method with standard error. Looking first at the $1/2^+$ channel in Fig. 6.9, I present a wave function with energy near the midpoint of the energy range examined, $E_{\text{c.m.}} = 2.85(2)$ MeV. For this channel and energy, I find close agreement between all methods. As expected from the ^{4}H results above, all overlap calculations agree at small radius. The integral method and GFMC propagation significantly change the VMC overlap in the outer parts of the box. Surprisingly, application of the integral method to the GFMC wave functions brings the overlap back into close alignment with the original VMC result.

For both $1/2^-$ (Fig. 6.10) and $3/2^-$ (Fig. 6.11) partial waves, considerable statistical variances are visible in the first few radial bins; this is due to evaluating derivatives (present in spin-orbit terms of the potential) of the unregularized irregular Coulomb function near the origin in Eq.(4.27). This does not affect scattering phase shifts because those come entirely from regularized integrals (Eq. (4.23)). For the $1/2^-$ scattering-state overlap in Fig. 6.10, the expected short-range agreement between direct and integral-method overlaps is visible. They diverge around 4 fm, similarly to the neutron-triton case. However, The $3/2^-$ overlaps in Fig. 6.11 show divergence between methods already at the shorter range of 2.5 — 3 fm.

Overall, the short-range spectroscopic overlaps agree reasonably well between direct and integral-method calculations within GFMC. This agreement suggests that it is safe to proceed with scattering calculations using the integral method in GFMC. As in the calculations of Chapter 6, I found that generating overlaps by the integral method and seeking reasonable levels of agreement with other calculations (VMC or direct) allowed identification and correction of multiple errors while extending the integral-method code for application to GFMC

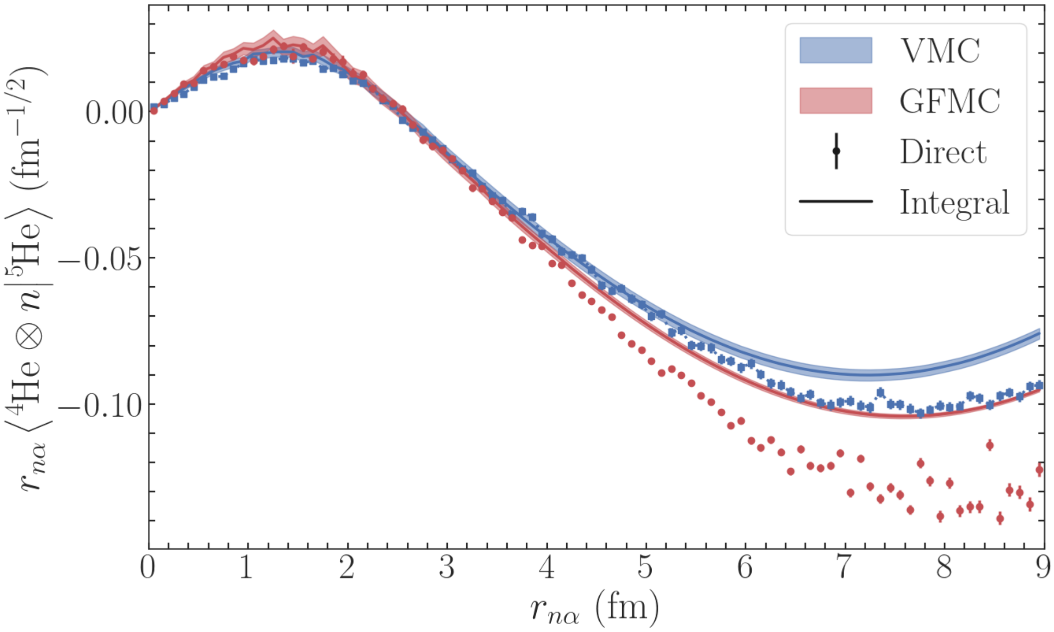

Figure 6.9: $n + {}^4$He overlaps as functions of alpha-neutron separation, computed from a representative $J^\pi = 1/2^+$ wave function with the AV18 interaction. These have been computed using the direct method of Eqs. (4.2) and (4.5) (circles with error bars) and the integral method of Eqs. (4.24) and (4.32) (solid curves with error bands) for VMC (blue) and GFMC (red) wave functions. The VMC overlaps were calculated using $E_{\mathrm{cm}} = 2.85(2)$ MeV, and the GFMC results were calculated at $E_{\mathrm{cm}} = 2.47(3)$ MeV. There is substantial agreement between all the methods for $r_{n\alpha} \leq 5$ fm.

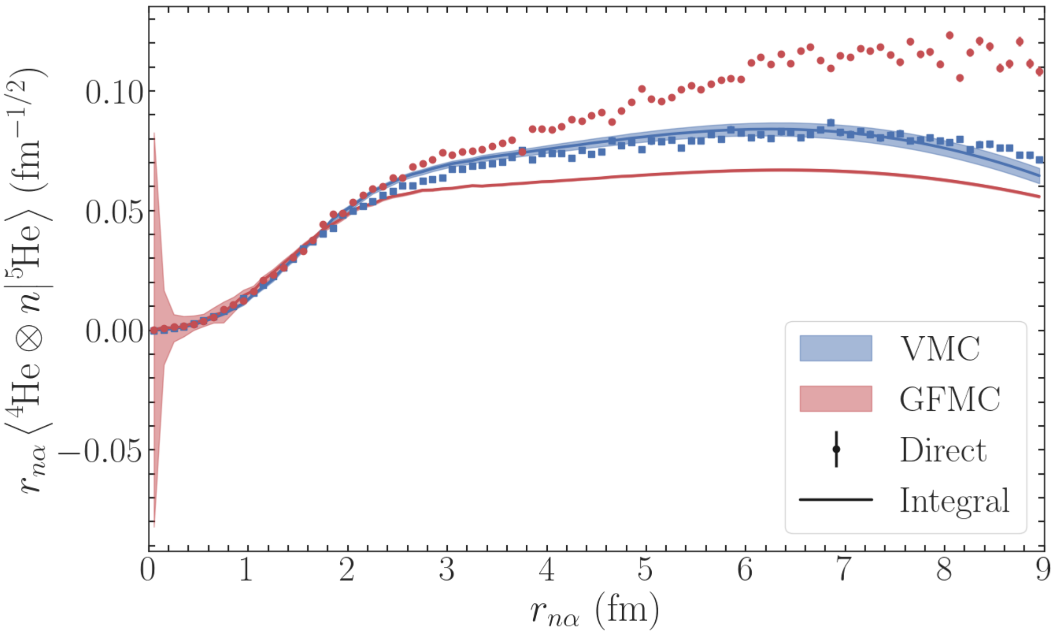

Figure 6.10: $n + {}^4\text{He}$ overlap functions computed from a representative $J^\pi = 1/2^-$ wave function with the AV18 interaction, analogous to Fig. 6.9. The VMC overlaps were calculated using $E_{\text{cm}} = 2.76(2)$ MeV, and the GFMC results were calculated using $E_{\text{cm}} = 2.35(3)$ MeV. Note the significant variance in the innermost bins due to the divergence of the irregular Coulomb function; regularization keeps this problem from affecting the computed phase shift. Away from the origin, overlaps computed with VMC wave functions agree with each other throughout the box. However, the GFMC calculations diverge from the VMC results and from each other outside the strong-interaction region (~ 3 fm, cf. the ^{4}He rms radius of 1.5 fm).

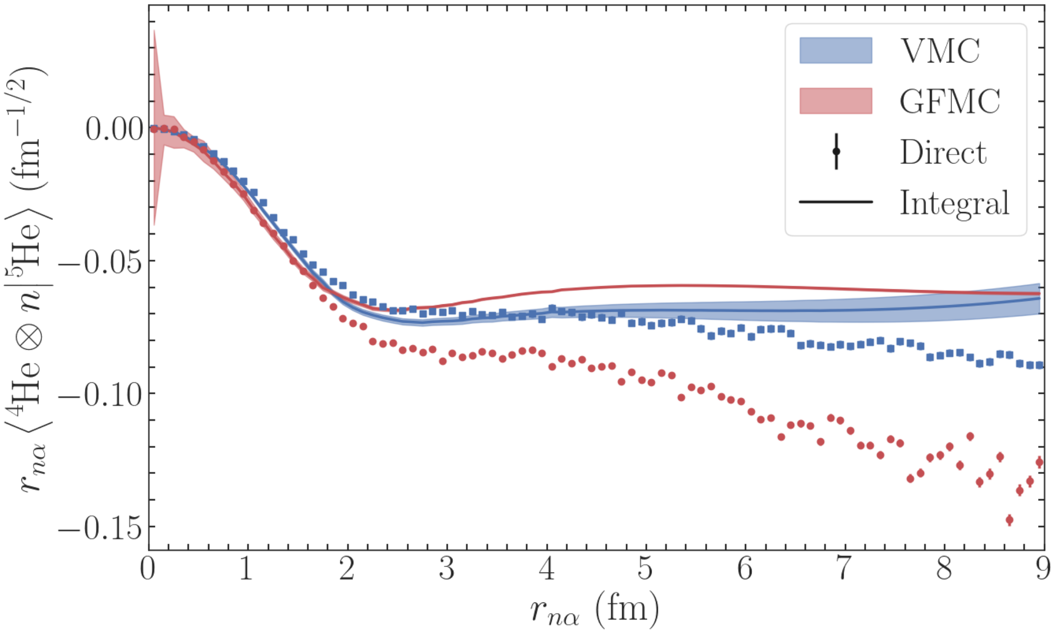

Figure 6.11: n+^{4}He overlap functions computed from a represtative $J^\pi = 3/2^-$ wave function with the AV18 interaction, analogous of Fig. 6.9. The VMC overlaps were calculated using $E_{\rm cm} = 1.55(3)$ MeV, and the GFMC results were calculated using $E_{\rm cm} = 1.04(3)$ MeV.

samples.

6.2.3 Single-channel phase shifts with the GFMC integral method

Once an energy has been computed for a state, Eq. (4.1) gives direct phase shifts. I also use GFMC samples generated during energy calculation to compute integral-method phase shifts. I begin by first looking at the s-wave ($1/2^+$) in Fig. 6.12. For each channel, I have three benchmarks for the phase shift; an R-matrix analysis of experimental data for the ^{5}He system (solid black curve) [80], a Faddeev-Yakubovsky calculation (solid squares) [10], and lastly, a careful direct-method GFMC calculation in which great caution was taken to limit dependence on the VMC starting point from ref. [25] (black diamonds). The two theoretical calculations are both based on the same AV18 interaction as those presented here. The difference between the current and previously-published direct GFMC calculations is that in the 2007 GFMC calculations, it was found necessary to iterate for self-consistent energy between the ϕ functions in the VMC starting point and the GFMC energy. I have not done that in the present work. However, the improvement in applying the boundary condition to $f_{sp}^{(A-1)}\phi$ discussed in Sec. 3.1.1 makes such iteration much less impactful. This is supported by the closeness of the two sets of direct GFMC points in Figs. 6.12, 6.14, and 6.16. Since the R-matrix curve is a fit to data, it is only presented for illustration; the accuracy of the integral method can only be judged by agreement with accurate calculations using the same potential. To my knowledge, the direct GFMC and the Faddev-Yakubovsky results are the only published *ab initio* n-alpha calculations using the AV18 potential. Although the authors of Ref. [10] claim convergence of their calculations at 5% precision in phase shift, their s-wave results fall somewhat below the trend of Ref. [25] by amounts that vary noticeably among their three points.

For the s-wave phase shifts in Fig. 6.12, I find that similarly to the $n + {}^3$H system, direct VMC (blue circles) provides a poor match to the previous careful GFMC results. However, direct GFMC (red circles) significantly corrects the phase shifts. Applying the integral method in VMC (blue squares) also significantly improves agreement with the previous GFMC calculations. Going from direct GFMC to integral-method GFMC phase shifts makes little difference at low energy. However, as energy increases, it produces more-positive phase shifts than the GFMC results from 2007.

In addition to including more physics through its direct use of the potential, the integral method allows use of the FIW approximation, reducing the effort needed to produce phase shifts of useful accuracy. Unlike the VMC FIW (blue dotted curves)calculations, the GFMC FIW (red dotted curves) in the neutron-alpha system gives an unexpectedly shallow slope for $\delta(E)$ in all channels for scattering energies above the energy of the wave function used. However, by using FIW as an interpolation scheme rather than an extrapolation scheme (FIWI see Sec. 5.2) we observe in Figs. 6.12, 6.14, and 6.16 that the interpolated phase

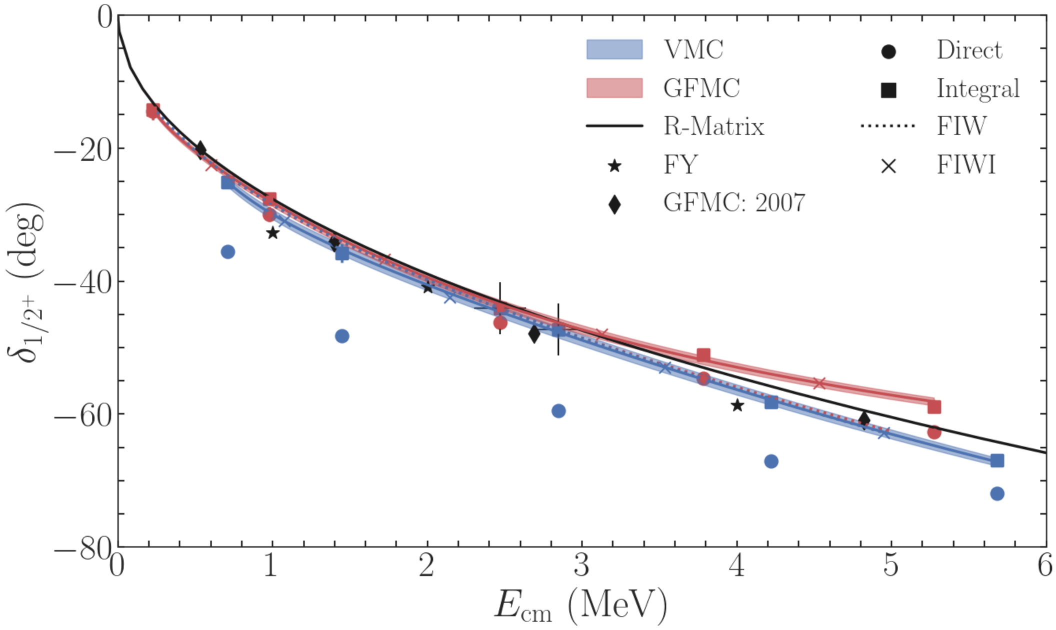

Figure 6.12: $J^\pi = 1/2^+$ phase shifts (in degrees) for $n + {}^4$He calculated with multiple methods using the AV18 interaction. The R-matrix phase shifts (black curve) are from Ref. [80]. The Faddeev-Yakubovsky AV18 phase shifts (black stars) are from Ref. [10]. The previously computed direct GFMC results (black diamonds) are from Ref. [25]. My current GFMC results are colored red, and VMC is colored blue. The direct method for both QMC methods is denoted with circles and the integral method with squares. I used the fixed interior wave approximation (dotted curves) to compute phase shifts using a single wave function marked with a "+" near the center of the computed energy range. I also use the FIW approximation to interpolate between my wave functions by averaging the K-matrix computed at the energy midpoint between any two wave functions; these interpolation points are marked with an "x." Lastly, the solid red and blue curves are fits of the squares and x's to ratios of quadratic polynomials.

shifts (VMC: blue X, GFMC: red X) follow the established trend of integral method GFMC results.

To better examine the trend of my computed phase shifts, I have fitted my results for the K-matrix ($K = \tan \delta_{J^\pi}$) to rational polynomials analogous to those used in Ref. [25] to locate S-matrix poles. I model $K(E) = p(E)/q(E)$, with p and q as quadratic polynomials whose coefficients are determined from a non-linear variance-weighted fitting procedure. I estimate the error in this fit as the mean percent error of the Monte Carlo calculations, which is around 1% for s-waves and 5 to 10% for p-waves. Without the FIWI, my computed grid of scattering energies is too sparse to constrain a ratio of cubic polynomials, and it would take more effort to obtain a smooth interpolant. To ease this problem I apply FIWI to add a point at the halfway point of each energy step in the plain integral-method calculation. Once I fit $\tan \delta_{J^\pi}$, I can quickly obtain phase shifts consistent with my integral-method calculations at any point within the computed energy range, and this is the solid curve (GFMC: red line, VMC: blue line) in Figs. 6.12, 6.14, and 6.16. This interpolation appears to produce a faithful representation of the computed integral-method results in all three partial waves. It is particularly useful in making differences between methods more visible in the graphs. In order to examine the VMC and GFMC integral method results, I have found it helpful to examine the K-matrix instead of the phase shift.

Moving on to the p-waves, I start by examining the $1/2^-$ channel phase shifts in Fig. 6.14 and $\tan \delta_{J^\pi}$ in Fig. 6.15. The integral method only helps VMC a little at the higher energies, though it is effective near threshold. Although the direct GFMC calculation was done less carefully here than in Ref. [25], the results are quite close except at the highest point. The GFMC integral-method phase shifts computed here are in reasonable agreement with Ref. [25]. They do differ noticeably from the direct phase shifts computed here, especially at that highest point. These results appear to conflict with the Faddeev-Yakubovsky results of Ref. [10]. This would seem to be caused by either a problem in the GFMC propagation

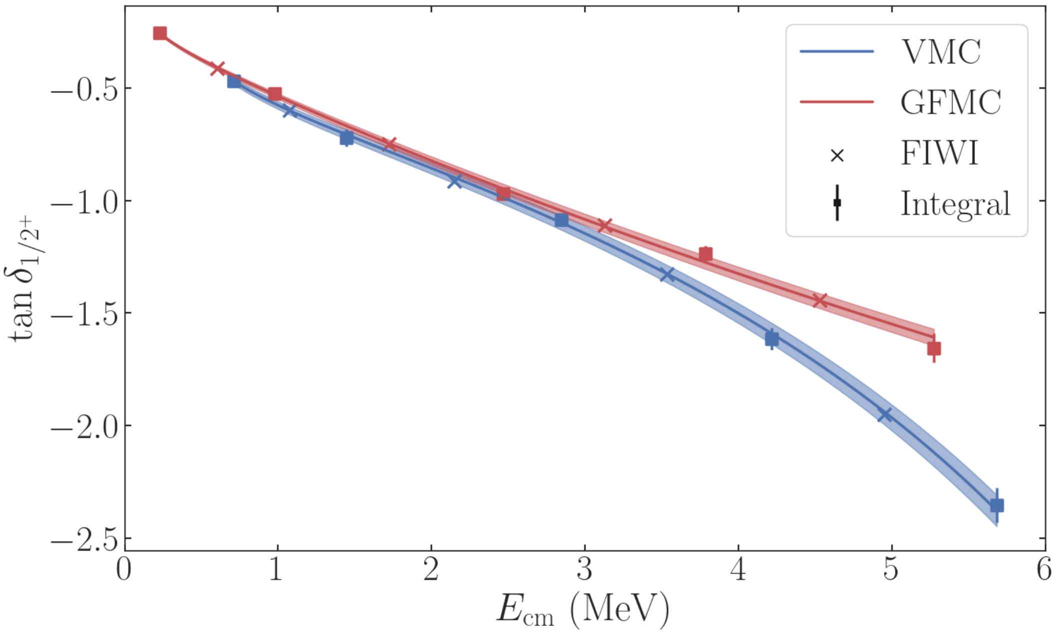

Figure 6.13: Computed values of $\tan\delta_{J^\pi}$ for $n + {}^4$He scattering in the $J^\pi = 1/2^+$ channel with the AV18 interaction. I evaluate the integral relations at the QMC energy for both GFMC (red) and VMC (blue) wave functions. Exact energy values are shown as squares, and the interpolated points are shown as x's, smooth curves are weighted fits to a ratio of quadratic polynomials.

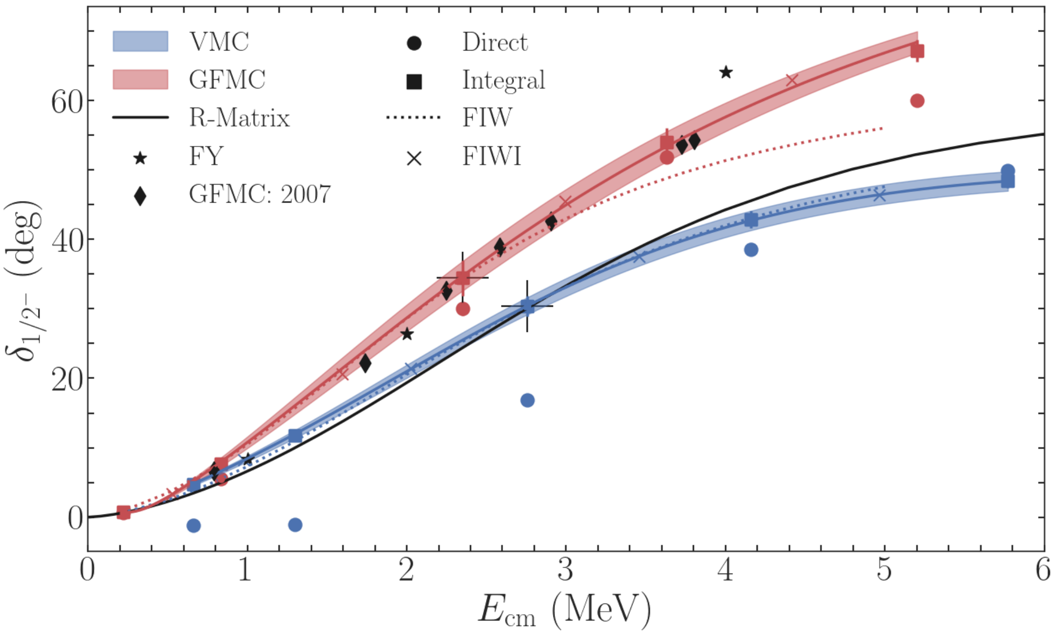

Figure 6.14: $J^\pi = 1/2^-$ phase shifts (in degrees) for $n+{}^4$He calculated with multiple methods using the AV18 interaction, analogous to Fig. 6.12.

(both here and in Ref. [25]) or overestimated convergence of the other group's three AV18 phase shifts in this channel.

The other p-wave, the $3/2^-$ channel, tells a slightly different story. In Fig. 6.16, all direct GFMC results, old and new, agree with each other and with the FY calculations within the error of the latter. However, the integral GFMC phase shifts tend to be larger than the other calculations in the neighborhood of 2.0 — 2.5 MeV, where the phase shift passes through 90°. We can see that the integral has difficulty near the resonance structure by analyzing the K-matrix in Fig. 6.17. The large variance near the discontinuity is related to the surface amplitude in the denominator of $\tan \delta_{J^\pi}$ going to zero; however, this variance indicates that better statistics might improve the phase shift calculations in this region. As with the other channels, direct VMC results produce phase shifts far from the other methods. Applying the integral method within VMC improves those results but does not bring them into an agreement with the GFMC.

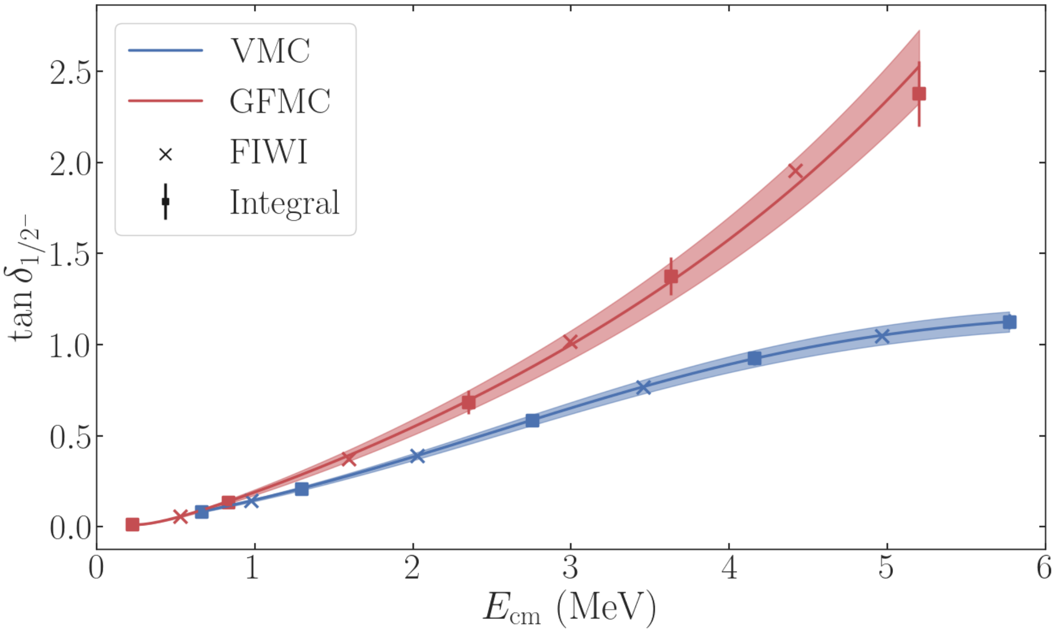

Figure 6.15: Computed values of $\tan\delta_{J^\pi}$ for $n+{}^4$He scattering in the $J^\pi = 1/2^-$ channel with the AV18 interaction, analogous to Fig. 6.13.

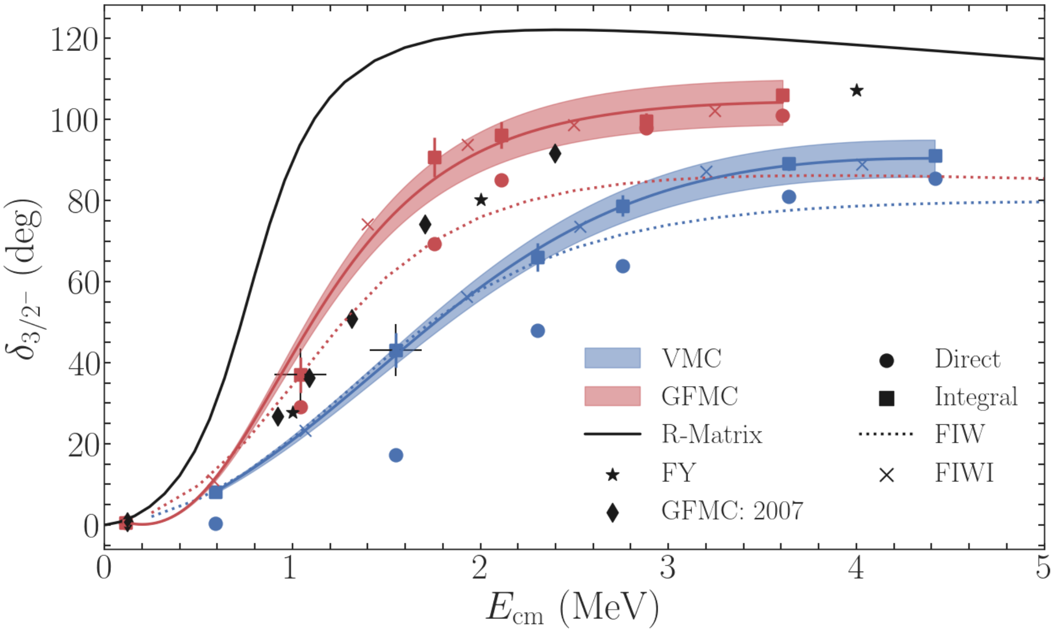

Figure 6.16: $J^\pi = 3/2^-$ phase shifts (in degrees) for $n+^4$He calculated with multiple methods using the AV18 interaction, analogous to Fig. 6.12. Note that the red integral-method point near 90° lies near a pole of $\tan\delta$, where the amplitude A goes to zero and causes the phase shift to have a large variance.

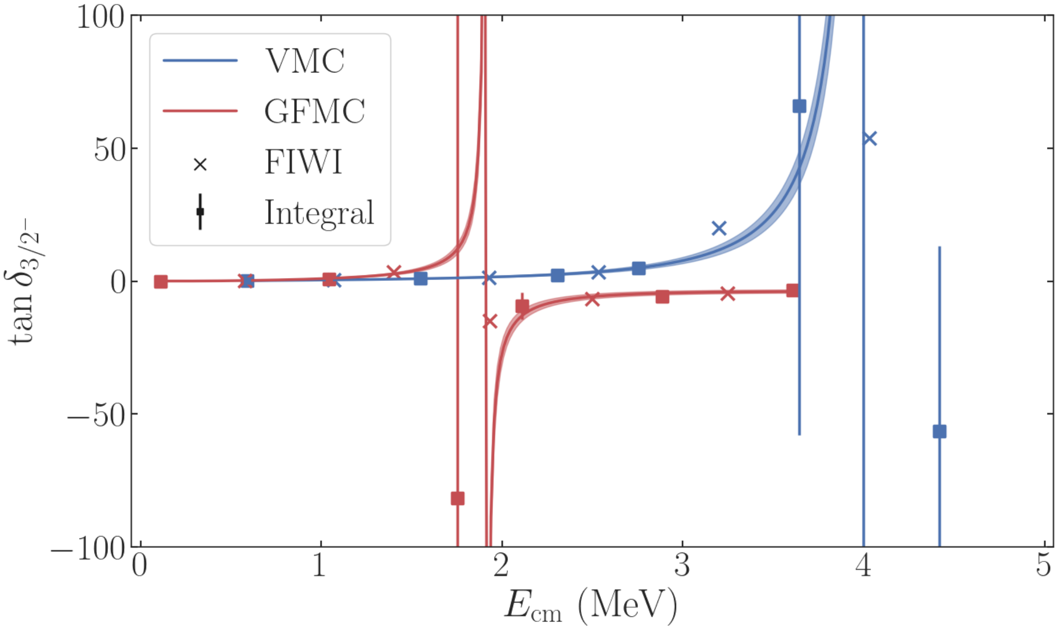

Figure 6.17: Computed values of $\tan\delta_{J^\pi}$ for $n+{}^4$He scattering in the $J^\pi = 3/2^-$ channel with the AV18 interaction, analogous to Fig. 6.13. The main feature of the $3/2^-$ channel is a strong resonance, which appears as a discontinuity in $\tan\delta$. Evaluating the integral relations near this discontinuity implies that the amplitude A approaches zero in the denominator of $\tan\delta = B/A$, which then diverges.

In summary, I have successfully implemented the integral method within GFMC and tested it out in neutron scattering from ^{4}He. Since I already believed direct GFMC to be accurate, it is no surprise that the integral method gives similar results. However, I have found some statistically significant differences that could be either improvements on the direct method or an unnoticed problem with the integral calculation. In either case, I have shown that the integral method works within GFMC and provides precision comparable to the direct calculation for single-channel scattering.

Chapter 7

Conclusion

I have successfully explored the use of the integral method to calculate scattering observables in the quantum Monte Carlo context. This method replaces operations on the most poorly computed parts of a VMC or GFMC wave function with integrals over the well-computed interaction region. They involve essentially matrix elements of the potential between the wave function and a cluster-product function in a specific channel. The integrand also contains regular and irregular scattering functions; the latter requires regularization to avoid difficulties arising from our use of Monte Carlo integration. Once that is done, the calculation within VMC can be carried out successfully with the customary $\Psi^\dagger\Psi$ weight function. The cost of calculation is close to the cost of an energy expectation value calculation once variational optimization is complete.

In every step of this work, I found it helpful to compute spectroscopic overlap functions using integral relations applicable at small radii. These could be computed from the same routines as the scattering integral relations and compared against directly-computed overlaps. This test of ensuring the integral method matched well onto the directly computed overlaps was an essential verification of the integral relation implementation in computer code at all stages.

I consistently used the overlap test to identify coding errors when developing the integral method for both VMC and GFMC, which is why I believe my scattering results. The overlaps also provided my only way of identifying regularizers that are unlikely to bias phase shift calculations. Since the regularization method is arbitrarily chosen, a crucial early task was identifying a good regularizer. My initial phase-shift calculations were only successful once I began measuring the accuracy of short-range overlap functions with the sum of square errors (SSE) heuristic, which measures the mismatch between methods of computing the short-range overlap.

In addition to developing the integral method, this work significantly improved the implementation of the scattering boundary condition, Eq. (3.9). Taking nucleon-nucleon correlations into account at the matching surface improved the accuracy of the boundary condition. That improved accuracy allowed better optimization of scattering wave functions, including automated variational minimization that was previously only useful for bound states. Further, I added substantial functionality to the energy-minimization search so that generation of new VMC wave functions is near fully automated for all systems. This functionality drastically reduces the human effort to calculate bound and unbound systems with many potentials, channels, and boundary conditions.

I have kept the computational expense of code development cheap by starting with some of the lightest systems that are interesting. The combination of well-benchmarked results and fast calculations allowed for quick development cycles, enabling internal tests to build confidence in my implementations. I first applied the integral method to variational Monte Carlo wave functions in both single- and coupled-channel problems for neutron scattering from tritium. The coupled channel cases are the first successful coupled channel calculations by any QMC method. I chose the $n + {}^3\mathrm{H}$ system as my initial test for the method because it is well benchmarked by nearly exact *ab initio* methods using nuclear potentials available to QMC, specifically the AV18 nucleon-nucleon interaction.

For all single-channel cases, the integral method with VMC provided a substantial improvement over phase shifts computed from the direct relationship between energy and the surface boundary condition. However, the important payoff for the integral method is the ease with which coupled channeled scattering can be computed. I explored the integral method for coupled channels in $n + {}^3$H, where results were better in some channels than others. The coupling of s-and d-waves reproduced the benchmark reasonably well. The coupling of singlet and triplet states in p-wave scattering resulted in a phase shift curve in one channel that is significantly different from the benchmark for unknown reasons, possibly related to the failure of linear independence between wave functions.

I also developed the integral method as an approximation technique away from the wave function energy in a procedure I call the fixed interior wave (FIW) approximation. In this approach, a single wave function is used in the integral relations, but varying energies are fed through the calculation. Tests of this method on VMC wave functions were reasonably successful in the neutron-triton. The FIW approximation demonstrates that reducing the effort to estimate cross sections over a substantial energy range is possible while retaining the established trend of integral method results.

In addition to testing the method against established benchmarks, I presented some of the only calculations done so far with the Norfolk potentials in nucleon-nucleus scattering. Although I computed scattering observables with Norfolk potentials only using VMC wave functions, the results provide valuable insight that is unavailable by only analyzing bound states. I found a stronger resonance structure for the Norfolk interactions in $n + {}^3$H than for AV18 + UIX in the p-wave channels. This difference is most visible in the larger Norfolk total $n + {}^3$H cross-section. By varying potentials, I found a 'Phillips line' relating the binding energy and neutron coherent scattering length of the triton with the same slope as that indicated by previous work, but offset by an amount that appears to reflect the accuracy of the VMC wave functions.

After completing my integral method calculations with VMC, I implemented the integral relations into the more accurate but expensive Green's function Monte Carlo (GFMC) method. This required the mixed-estimate calculation of essentially a matrix element of the potential, but the code was not written to allow application of the potential to cluster-product functions. The calculation required that I write a second implementation of the potential operator to do this. Since the spin-isospin states needed for most neutron-triton scattering channels do not yet exist in the GFMC code, I tested the integral method's implementation on neutron-alpha scattering calculations using the AV18 potential.

The only extensive calculations of this system with potentials available to the GFMC method were, in fact, also carried out in GFMC in an earlier version of the same code. Direct calculations that I carried out agreed with those earlier calculations in most cases. Although this left little room for the integral relations to improve the results (unlike the VMC case), I verified that the integral relation produced consistent results. In some cases, there was slight disagreement with the older calculations, suggesting minor difficulty with the method. In future applications that involve coupled channels, a loss of accuracy on that level is an acceptable trade-off for being able to carry out the calculation.

For my n+alpha calculations, I extended the FIW approximation to develop it as an interpolation scheme I call fixed interior wave interpolation (FIWI). This procedure aims to improve FIW results by applying FIW to wave functions at higher and lower energy than the desired energy and averaging the results. I found some minor difficulties with the FIW for energies above the computed wave functions energy expectation value, the FIWI was successful in resolving this problem.

Overall, the integral method substantially improves scattering observables when applied to VMC compared to previously used methods. However, for GFMC, in most cases the integral method only maintains the accuracy previously achieved and, in some cases, has difficulties reproducing benchmarked results. The critical trade-off is that the integral method paves the way for coupled-channel scattering in GFMC. Thus, the integral method provides a clear path for single-nucleon scattering well into the p-shell ($A \leq 10$). For comparable *ab initio* methods, these larger nuclei and even $A = 5$ can be challenging to obtain converged results for local potentials, primarily due to the exponential computational cost. If these larger scattering systems are computed with local potentials, it will be an excellent achievement for QMC and the field.

With GFMC-accurate coupled channel scattering just around the corner, prospects are suitable for a broader range of accurate *ab initio* calculations of reactions and scattering at mass ranges beyond the mass-four systems. The integral method opens the door to a predictive framework for bound and unbound nuclei that eludes generating system-dependent models. Specifically, it is immediately possible to compute $T = 0$ states in ^{4}He with excited states treated as actual scattering states, which the calculation recently attained renewed focus. It will also be possible with further work to calculate electromagnetic and weak capture reactions, which will be of significant astrophysical interest; as some of those reactions cannot be carried out in the laboratory. Lastly, with significantly more effort, it may be possible to compute reactions with nuclear rearrangement. The ability to compute these reactions in a general predictive framework would be a pinnacle accomplishment in our capacity to model the world.

Bibliography

[1] C. W. Johnson, K. D. Launey, N. Auerbach, S. Bacca, B. R. Barrett, C. R. Brune, M. A. Caprio, P. Descouvemont, W. H. Dickhoff, C. Elster, P. J. Fasano, K. Fossez, H. Hergert, M. Hjorth-Jensen, L. Hlophe, B. Hu, R. M. I. Betan, A. Idini, S. König, K. Kravvaris, D. Lee, J. Lei, A. Mercenne, R. N. Perez, W. Nazarewicz, F. M. Nunes, M. Ploszajczak, J. Rotureau, G. Rupak, A. M. Shirokov, I. Thompson, J. P. Vary, A. Volya, F. Xu, R. G. T. Zegers, V. Zelevinsky, and X. Zhang, J. Phys. G **47**, 123001 (2020).

[2] D. Bazin, K. Becker, F. Bonaiti, C. Elster, K. Fossez, T. Frederico, A. Gnech, C. Hebborn, M. Higgins, L. Hlophe, B. Kay, S. König, K. Kravvaris, J. Lubian, A. Macchiavelli, F. Nunes, L. Platter, G. Potel, and X. Zhang, Few-Body Syst. **64**, 25 (2023).

[3] M. Viviani, A. Deltuva, R. Lazauskas, J. Carbonell, A. C. Fonseca, A. Kievsky, L. Marcucci, and S. Rosati, Phys. Rev. C **84**, 054010 (2011).

[4] M. Viviani, A. Deltuva, R. Lazauskas, A. C. Fonseca, A. Kievsky, and L. E. Marcucci, Phys. Rev. C **95**, 034003 (2017).

[5] R. Lazauskas and J. Carbonell, Phys. Rev. C **70**, 044002 (2004).

[6] R. Lazauskas, J. Carbonell, A. C. Fonseca, M. Viviani, A. Kievsky, and S. Rosati, Phys. Rev. C **71**, 034004 (2005).

[7] R. Lazauskas, Phys. Rev. C **79**, 054007 (2009).

[8] R. Lazauskas, Phys. Rev. C **86**, 044002 (2012).

[9] R. Lazauskas, Phys. Rev. C **97**, 044002 (2018).

[10] R. Lazauskas and J. Carbonell, Front. Phys. **7** (2020).

[11] A. Deltuva and A. C. Fonseca, Phys. Rev. Lett. **113**, 102502 (2014).

[12] A. Deltuva and A. C. Fonseca, Phys. Lett. B **742**, 285 (2015).

[13] A. Deltuva and A. C. Fonseca, Phys. Rev. C **92**, 024001 (2015).

[14] A. Deltuva and A. C. Fonseca, Phys. Rev. C **91**, 034001 (2015).

[15] A. Deltuva and A. C. Fonseca, Phys. Rev. C **95**, 024003 (2017).

[16] E. O. Alt, W. Sandhas, and H. Ziegelmann, Phys. Rev. C **17**, 1981 (1978).

[17] E. O. Alt and W. Sandhas, Phys. Rev. C **21**, 1733 (1980).

[18] A. Deltuva, A. C. Fonseca, and P. U. Sauer, Phys. Rev. C **72**, 054004 (2005).

[19] A. Deltuva, A. C. Fonseca, and P. U. Sauer, Phys. Rev. Lett. **95**, 092301 (2005).

[20] A. Kievsky, S. Rosati, M. Viviani, L. E. Marcucci, and L. Girlanda, J. Phys. G **35**, 063101 (2008).

[21] L. E. Marcucci, A. Kievsky, L. Girlanda, S. Rosati, and M. Viviani, Phys. Rev. C **80**, 034003 (2009).

[22] P. Barletta, C. Romero-Redondo, A. Kievsky, M. Viviani, and E. Garrido, Phys. Rev. Lett. **103**, 090402 (2009).

[23] A. Kievsky, M. Viviani, P. Barletta, C. Romero-Redondo, and E. Garrido, Phys. Rev. C **81**, 034002 (2010).

[24] M. Viviani, L. Girlanda, A. Kievsky, and L. E. Marcucci, Phys. Rev. C **102**, 034007 (2020).

[25] K. M. Nollett, S. C. Pieper, R. B. Wiringa, J. Carlson, and G. M. Hale, Phys. Rev. Lett. **99**, 022502 (2007).

[26] J. Carlson, S. Gandolfi, F. Pederiva, S. C. Pieper, R. Schiavilla, K. E. Schmidt, and R. B. Wiringa, Rev. Mod. Phys. **87**, 1067 (2015).

[27] M. Piarulli, I. Bombaci, D. Logoteta, A. Lovato, and R. B. Wiringa, Phys. Rev. C **101**, 045801 (2020).

[28] A. Lovato, I. Bombaci, D. Logoteta, M. Piarulli, and R. B. Wiringa, Phys. Rev. C **105**, 055808 (2022).

[29] J. Carlson, V. R. Pandharipande, and R. B. Wiringa, Nucl. Phys. A **424**, 47 (1984).

[30] J. Carlson, K. E. Schmidt, and M. H. Kalos, Phys. Rev. C **36**, 27 (1987).

[31] J. E. Lynn, I. Tews, J. Carlson, S. Gandolfi, A. Gezerlis, K. E. Schmidt, and A. Schwenk, Phys. Rev. Lett. **116**, 062501 (2016).

[32] W. T. Pinkston and G. R. Satchler, Nucl. Phys. **72**, 641 (1965).

[33] M. Kawai and K. Yazaki, Prog. Theor. Phys. **38**, 850 (1967).

[34] A. Mukhamedzhanov and N. Timofeyuk, Sov. J. Nucl. Phys. **51**, 431 (1990).

[35] N. K. Timofeyuk, Nucl. Phys. A **632**, 19 (1998).

[36] N. K. Timofeyuk, Phys. Rev. C **81**, 064306 (2010).

[37] K. M. Nollett and R. B. Wiringa, Phys. Rev. C **83**, 041001 (2011).

[38] K. M. Nollett, Phys. Rev. C **86**, 044330 (2012).

[39] F. E. Harris, Phys. Rev. Lett. **19**, 173 (1967).

[40] C. Romero-Redondo, E. Garrido, P. Barletta, A. Kievsky, and M. Viviani, Phys. Rev. A **83**, 022705 (2011).

[41] I. Brida, S. C. Pieper, and R. B. Wiringa, Phys. Rev. C **84**, 024319 (2011).

[42] L. S. Rodberg and R. M. Thaler, *Introduction to the Quantum Theory of Scattering* (Academic Press, New York, 1967).

[43] A. B. Olver, F. W. J.and Olde Daalhuis, D. W. Lozier, B. I. Schneider, R. F. Boisvert, C. W. Clark, B. R. Miller, S. B. V., H. S. Cohl, and M. A. McClain, "NIST Digital Library of Mathematical Functions," http://dlmf.nist.gov/, Release 1.1.6 of 2022-06-30 (2022).

[44] J. M. Blatt and L. C. Biedenharn, Rev. Mod. Phys. **24**, 258 (1952).

[45] R. G. Newton, *Scattering Theory of Waves and Particles*, 2nd ed. (Springer-Verlag, New York, 1982).

[46] T. W. Phillips, B. L. Berman, and J. D. Seagrave, Phys. Rev. C **22**, 384 (1980).

[47] J. A. Carlson and R. B. Wiringa, in *Computational Nuclear Physics 1: Nuclear Structure*, edited by K. Langanke, J. A. Maruhn, and S. E. Koonin (Springer Berlin Heidelberg, Berlin, Heidelberg, 1991) pp. 171–189.

[48] B. S. Pudliner, V. R. Pandharipande, J. Carlson, S. C. Pieper, and R. B. Wiringa, Phys. Rev. C **56**, 1720 (1997).

[49] I. E. Lagaris and V. R. Pandharipande, Nucl. Phys. A **359**, 349 (1981).

[50] R. B. Wiringa, AIP Conf. Proc. **1128**, 1 (2009).

[51] R. B. Wiringa, Phys. Rev. C **43**, 1585 (1991).

[52] http://ab-initio.mit.edu/wiki/index.php/NLopt, (Accessed: Jan. 2021).

[53] J. Carlson, V. R. Pandharipande, and R. B. Wiringa, Nucl. Phys. A **401**, 59 (1983).

[54] K. M. Nollett, R. B. Wiringa, and R. Schiavilla, Phys. Rev. C **63**, 024003 (2001).

[55] K. M. Nollett, Phys. Rev. C **63**, 054002 (2001).

[56] R. Schiavilla and R. B. Wiringa, Phys. Rev. C **65**, 054302 (2002).

[57] S. C. Pieper, Riv. Nuovo Cimento **31**, 709 (2009).

[58] B. S. Pudliner, V. R. Pandharipande, J. Carlson, and R. B. Wiringa, Phys. Rev. Lett. **74**, 4396 (1995).

[59] S. Zhang, J. Carlson, and J. E. Gubernatis, Phys. Rev. B **55**, 7464 (1997).

[60] R. B. Wiringa, S. C. Pieper, J. Carlson, and V. R. Pandharipande, Phys. Rev. C **62**, 014001 (2000).

[61] M. Pervin, S. C. Pieper, and R. B. Wiringa, Phys. Rev. C **76**, 064319 (2007).

[62] G. B. King, L. Andreoli, S. Pastore, and M. Piarulli, Front. Phys. **8** (2020).

[63] J.Carlson unpublished notes (2006).

[64] S. C. Pieper and R. B. Wiringa, Annu. Rev. of Nucl. and Part. Sci. **51**, 53 (2001).

[65] G. Satchler, *Direct nuclear reactions* (Oxford University Press, Oxford, New York, 1983).

[66] S. Cohen and D. Kurath, Nuclear Physics A **101**, 1 (1967).

[67] L. Lapikás, J. Wesseling, and R. B. Wiringa, Phys. Rev. Lett. **82**, 4404 (1999).

[68] L. E. Marcucci, J. Dohet-Eraly, L. Girlanda, A. Gnech, A. Kievsky, and M. Viviani, Front. Phys. **8** (2020).

[69] R. J. Philpott, W. T. Pinkston, and G. R. Satchler, Nucl. Phys. A **119**, 241 (1968).

[70] G. M. Hale, D. C. Dodder, J. D. Seagrave, B. L. Berman, and T. W. Phillips, Phys. Rev. C **42**, 438 (1990).

[71] M. Piarulli, A. Baroni, L. Girlanda, A. Kievsky, A. Lovato, E. Lusk, L. E. Marcucci, S. C. Pieper, R. Schiavilla, M. Viviani, and R. B. Wiringa, Phys. Rev. Lett. **120**, 052503 (2018).

[72] A. Baroni, R. Schiavilla, L. E. Marcucci, L. Girlanda, A. Kievsky, A. Lovato, S. Pastore, M. Piarulli, S. C. Pieper, M. Viviani, and R. B. Wiringa, Phys. Rev. C **98**, 044003 (2018).

[73] A. Aurdal, Nucl. Phys. A **146**, 385 (1970).

[74] R. Crespo, A. Arriaga, R. Wiringa, E. Cravo, A. Mecca, and A. Deltuva, Phys. Lett. B **803**, 135355 (2020).

[75] D. A. Brown, M. B. Chadwick, R. Capote, A. C. Kahler, A. Trkov, M. W. Herman, A. A. Sonzogni, Y. Danon, A. D. Carlson, M. Dunn, *et al.*, Nucl. Data Sheets **148**, 1 (2018).

[76] S. Hammerschmied, H. Rauch, H. Clerc, and U. Kischko, Z. Phys. A **302**, 323 (1981).

[77] H. Rauch, D. Tuppinger, H. Wölwitsch, and T. Wroblewski, Phys. Lett. B **165**, 39 (1985).

[78] M. Wang, G. Audi, A. H. Wapstra, F. G. Kondev, M. MacCormick, X. Xu, and B. Pfeiffer, Chinese Phys. C **36**, 1603 (2012).

[79] J. Kirscher, Phys. Lett. B **721**, 335 (2013).

[80] G. M. Hale, D. C. Dodder, and K. Witte, Unpublished.